https://doi.org/10.5194/egusphere-2026-729
Preprint. Discussion started: 3 March 2026

Mass changes of the Antarctic Peninsula ice sheet and peripheral glaciers, 2007−2021

Maud Bernat[1], Etienne Berthier[1], Amaury Dehecq[2], Romain Hugonnet[3], Joaquin MC Belart[4], Naomi Ochwat[5, 7], Peter Kuipers Munneke[6], Elizabeth Case[6], Ted Scambos[7], Louis-Marie Gauer[1], and David Youssefi[8]

[1]Université de Toulouse, LEGOS (CNES/CNRS/IRD/UT3), Toulouse, France
[2]Laboratoire de Glaciologie et Géophysique de l'Environnement, Grenoble, France
[3]Geophysical Institute, University of Alaska Fairbanks, Fairbanks, Alaska, USA
[4]Natural Science Institute of Iceland, Akranes, Iceland
[5]University of Innsbruck, Innsbruck, Austria
[6]University of Utrecht, Institute of Marine and Atmospheric Research Utrecht, Utrecht, Netherlands
[7]Earth Science Observation Center, Cooperative Institute for Research in Environmental Science, University of Colorado Boulder, Boulder, CO, USA
[8]Centre National des Etudes Spatiales, Toulouse, France

Correspondence: Maud Bernat (maud.bernat@utoulouse.fr)

Abstract. The Antarctic Peninsula (AP), encompassing the ice sheet and its peripheral glaciers, is a highly dynamic component of the cryosphere that disproportionately contributes to sea-level rise relative to its size. However, a large spread remains between the mass changes estimated using gravimetry, altimetry and the mass budget method. Among these techniques, the satellite (radar or laser) altimetry method has a resolution of, at best, 1 km, which is too coarse to resolve the mountainous landscape of the Peninsula. Therefore, we use digital elevation models (DEMs; 30 x 30 m) to provide an estimate of mass changes across the AP between 2007 and 2021. We combine 476 DEMs derived from SPOT5-HRS satellite images (2006−2008) and 2 525 DEMs of the Reference Elevation Model of Antarctica (2020−2022) to map elevation changes for the entire Peninsula. We vertically adjusted each DEM using near-coincident ICESat/-2 laser altimetry measurements. Our observations cover 70% of the AP Ice Sheet and 60% of its peripheral glaciers, including regions of the Peninsula poorly studied to date, and reveal a spatially complex pattern of elevation changes. After correction with different models of firn air content and solid-earth response, we find that between 2007 and 2021, the AP Ice Sheet lost -27 ± 9 Gt/a while its peripheral glaciers lost -14 ± 2 Gt/a. For the AP Ice Sheet, our new estimate is 4 to 5 times more negative than the one obtained in IMBIE using altimetry data (-5.2 ± 2.3 Gt/a from 2007 to 2019) and in better agreement with gravimetry and the mass budget method. Our study highlights the importance of resolving fine scale elevation changes of glaciers and ice sheets in complex, dynamic coastal areas.

1 Introduction

The Antarctic Peninsula, covering an area of 335 000 km^2 (Silva et al., 2020), is a mostly narrow and mountainous region, characterized by a high altitude plateau that predominantly feeds marine terminating glaciers (Fig. 1a). The Antarctic Peninsula Ice Sheet (APIS) is surrounded by numerous islands partly covered by ice that are independent from the mainland, referred herein as the peripheral glaciers (Pfeffer et al., 2014). Climate conditions vary greatly across the AP, with mild weather and high snowfall in the west, and drier and colder conditions in the east, where most ice shelves are found (Orr et al., 2008). In the context of climate change, the AP ice masses are responding dynamically. The region encompasses many of Antarctica's rapidly changing glaciers; these changes are often linked to the thinning or breakup of their ice-shelves, e.g. Drygalski, Hektoria, and Crane glaciers (Davison et al., 2023). Although the APIS constitutes only 4% of the total area of the whole continent and 0.5% of the total ice volume (extracted from Pritchard et al., 2025), it represented ∼15% of Antarctica's total glacier mass loss between 1992 and 2020 (Otosaka et al., 2023). Both tidewater and ice-shelf tributary glaciers of the AP are projected to significantly contribute to sea-level rise, caused by complex dynamic responses to climate change (Schannwell et al., 2016).

Previous studies have estimated the mass evolution of the APIS at various timescales, from multidecadal (e.g. Nilsson et al., 2022; Rignot et al., 2019) to short-term changes (e.g. Seehaus et al., 2023; Wouters et al., 2015). Three main methods are used to study the mass changes of the polar ice-sheets, including the APIS: gravimetry, the mass-budget method (also called the input-output method) and the elevation-differencing method, based on laser or radar altimetry. Estimates have been calculated regularly (Otosaka et al., 2023; Shepherd et al., 2018) and show a large spread in inferred mass loss, especially for the APIS. For example, over the period 2007−2019, mass changes ranging from -5.2 ± 2.3 Gt/a (altimetry) to -41.7 ± 5.7 Gt/a (mass budget method) were estimated for this region (adapted from Otosaka et al., 2023). All these methods, providing APIS-wide estimates, do not resolve fine-scale processes.

Elevation differencing has been extensively applied to the AP using sparse satellite altimetry measurements but rarely from digital elevation models (DEMs). The DEM-differencing method has been used to study very localized sites (e.g. Zhao et al., 2017), occasionally providing multidecadal time series (e.g. Kunz et al., 2012). When applied to larger subregions of the AP, it was limited to short time periods ($\leq$ 5 years, e.g. Seehaus et al., 2023; Scambos et al., 2014; Rott et al., 2018). Here, we investigate the mass changes of all AP glaciers using the DEM-differencing method. DEMs can provide elevation information at high spatial resolution (20−100 m) across areas of thousands of square kilometers. However, openly available DEM datasets, derived either from optical or radar sensors, are not available at annual resolutions for the entire AP. This is due to frequent and persistent cloud-cover hindering optical acquisitions, and the difficulty of unwrapping the phase of radar images due to the region's steep topography. Depending on the acquisition technique, DEMs have different limitations: radar-based DEMs often have firn penetration biases (Bannwart et al., 2024; Rott et al., 2021), while DEMs from optical stereoscopic imagery are affected by lack of contrast in very dark (e.g. shadows) and very bright (e.g. fresh snow) areas (Noh and Howat, 2015). Furthermore, any elevation differencing method requires the use of external models to correct first-order elevation changes for physical processes that affect surface height but not ice mass. These include firn densification, glacial isostatic adjustment (GIA) and elastic rebound (ELR). The inclusion of these models can introduce large uncertainties into this method.

In this study, we provide a new estimate of the mass changes of the entire AP between 2007 and 2021, covering the APIS and its peripheral glaciers (Hock et al., 2023). We used only optical imagery and laser altimetry to avoid signal penetration effects.

We generated nearly complete topography for 2006−2008 from the SPOT5-HRS archive (Satellite pour l'Observation de la Terre, High Resolution Stereoscopic) that we compared to REMA DEMs (Reference Elevation Model of Antarctica, Howat et al., 2022b) from 2020−2022. Both stereoscopic datasets were vertically adjusted on near-coincident laser altimetry data (ICESat and ICESat-2—Ice, Cloud, and land Elevation Satellite), resulting in an excellent vertical precision for the elevation difference maps, typically half a meter per year per pixel. We calculated maps of elevation difference rates over the 14-year period 2007−2021 that we corrected with different models of firn air content (FAC), GIA and elastic rebound to obtain mass changes for the entire AP.

2 Data

This study focuses on two epochs, each corresponding to three consecutive austral summers, defined as the period from October of the previous year to March of the given year. The first epoch is centered on 2007, including austral summers of 2006, 2007 and 2008, and the second one is centered on 2021, including austral summers of 2020, 2021 and 2022. We used elevation data from two types of measurements, stereoscopic imagery and laser altimetry, defined in the polar stereographic coordinate system (EPSG 3031). Data sources differ between the two epochs: for the first, we used ICESat for laser altimetry and SPOT5-HRS for the DEMs, and for the latter we used ICESat-2 and REMA. To prevent potential seasonal biases, we selected seasonally coherent data (2-month maximum interval not considering the year difference) when comparing elevations between the two epochs (unless noted otherwise). The temporal distribution of the elevation datasets is shown in Fig. 2.

2.1 Stereoscopic imagery

SPOT5-HRS archive

SPOT5 is an optical satellite that was operated between May 2002 and March 2015. It was equipped with the HRS sensor that acquired image pairs in panchromatic mode (0.48−0.71 μm). Stereoscopic pairs were acquired in a single pass of the satellite, 90 seconds apart, limiting the potential changes between the two images. The sensor was also characterized by a large 120-km swath and rectangular 5-m x 10-m pixels (along-track x cross-track) (Bouillon et al., 2006). As part of the SPIRIT program (SPOT5 stereoscopic survey of Polar Ice: Reference Images and Topographies, Korona et al., 2009), the Antarctic Peninsula was surveyed during the austral summers of 2006, 2007 and 2008 (Fig. 2). The data recorded by HRS used 8-bit encoding, which only allows for 256 different gray-levels. This is one of the main limitations of this sensor in glaciological studies where ice and snow surfaces, that are highly reflective, can produce saturated pixels (Berthier et al., 2023). To help mitigate this effect, during the SPIRIT program, the sensor gains were adapted every week to ensure good contrast over ice sheets surfaces relative to the time of year and latitude. In 2021, all the SPOT5-HRS data archive was made publicly accessible through the CNES Spot World Heritage Program.

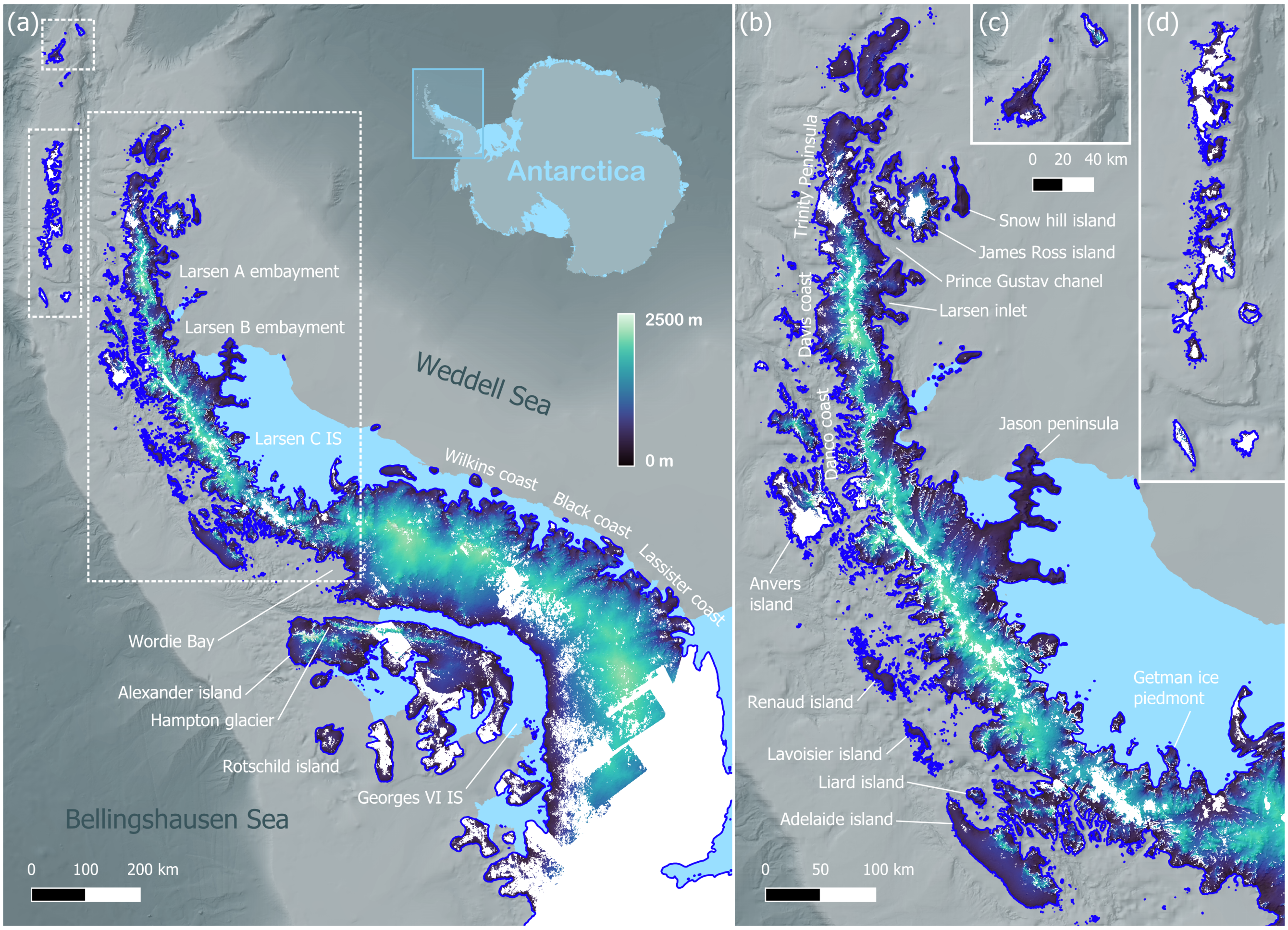

Figure 1. Spatial coverage obtained from SPOT5-HRS archive over the Antarctic Peninsula (2006-2008). Terrain with SPOT5-HRS data coverage colored, while gaps are shown in white. Grounded ice and ice shelves (IS) outlines are plotted as thick blue line and light blue respectively, while the bathymetry is shown as a colored hillshade Pritchard et al. (2025). (a) shows the HRS DEMs coverage on the entire AP. (b), (c) and (d) correspond to the insets indicated as white boxes on (a), zooming on the northern part of the APIS (b) and the South Shetland Islands (c) and (d). We included the names of the main geographical features cited in the text.

Reference Elevation Model of Antarctica

The REMA project was created to produce the first gapless DEM of Antarctica at high spatial resolution (Howat et al., 2019). Sub-meter stereoimages were acquired by four commercially operated satellites: GeoEye-1 (from 2008, 15.2 km swath), WorldView-1 (from 2007, 17.6 km swath), WorldView-2 (from 2009, 16.4 km swath) and WorldView-3 (from 2014, 13 km swath). For each available stereopair, a DEM was generated (Noh and Howat, 2017) at 2-m pixel resolution. Due to the high spatial and radiometric resolution of the stereoscopic images, even areas with low contrast terrains, like snow, ice and shadows, could be measured. Time-stamped DEMs and their associated binary masks (pixel validity) are publicly available at a 2-m

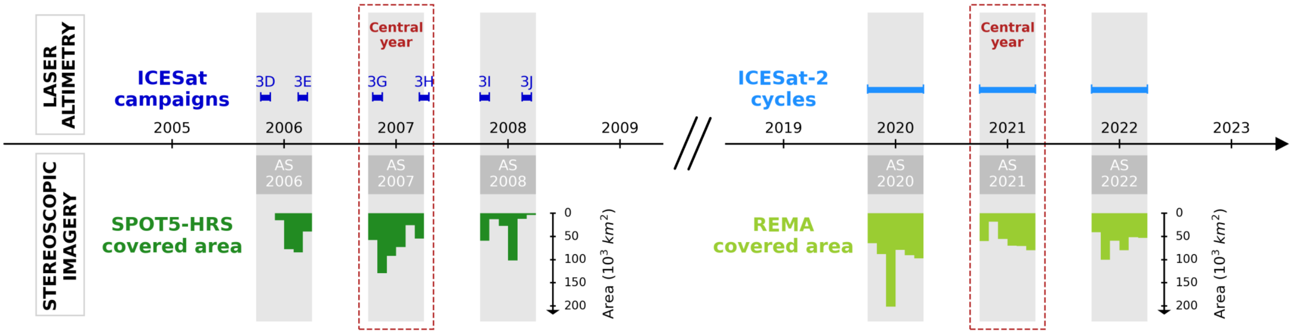

Figure 2. Timeline of the elevation datasets. For the first epoch (2006−2008), monthly SPOT5-HRS covered area is indicated in dark green and ICESat campaigns duration in dark blue. For the second epoch (2020−2022), monthly REMA covered area is indicated in light green and the ICESat-2 extracted periods in light blue. AS stands for austral summer.

pixel resolution (Howat et al., 2022b). We used REMA DEMs acquired during the austral summers of 2020, 2021 and 2022, to match the seasonal characteristics of HRS acquisitions. These years were selected because they had the most acquisitions over the AP compared to later years.

2.2 Laser altimetry

ICESat

ICESat was launched by NASA in 2003, primarily to monitor the mass change of the ice sheets (Zwally et al., 2002). Until 2009, elevation data was collected from the GLAS (Geoscience Laser Altimeter System) instrument over Greenland and Antarctica, with a polar orbit up to 88° north and south. Laser pulses of 1064-nm wavelength (infrared) were used to measure surface heights with an along-track sampling interval of 172 m and a footprint diameter of 60 m. Due to unexpected laser malfunctions, the initially continuous operation mode was converted into 9 campaigns of 8 to 37 days every three to six months (Schutz et al., 2005). To match the SPOT5-HRS temporal coverage (2006-2008), we selected the high energy campaigns 3D, 3E, 3G, 3H, 3I and 3J (Fig. 2). We used the GLA12 Records Release 34 ice sheets elevation product (Zwally et al., 2014).

ICESat-2

Building on the legacy of ICESat, the ICESat-2 mission was designed to extend and improve the elevation measurements from space-borne laser altimetry (Markus et al., 2017). The satellite began operations in September 2018 on the same orbit as its predecessor (88° north and south) and is still operational in 2026, with a repeat cycle of 91 days. The Advanced Topographic Laser Altimeter System (ATLAS) carries three pairs of laser beams that measure the surface height, enabling slope effect correction and increasing spatial coverage. The photon counting detectors also improved the along-track spatial sampling to 0.7 m with a footprint diameter of 17 m. For glaciological purposes, we used the ATL06 product Land Ice Elevation at 40-m along

https://doi.org/10.5194/egusphere-2026-729
Preprint. Discussion started: 3 March 2026

track resolution. In line with the epoch of REMA DEMs, we retrieved ICESat-2 data for the austral summers of 2020, 2021 and 2022 (Fig. 2).

2.3 Glacial catchment outlines

We selected four distinct glacier outline datasets for different purposes. Firstly, we used the outlines of glacial catchments and rock outcrops from Silva et al. (2020). We refer to the outlines from this study as SIL20. This dataset includes peripheral glaciers disconnected from the ice sheet and the glacial catchments of the APIS, resulting in a total of 1 855 glaciers. Secondly, to ensure that our results are comparable with other studies, we also used three standard outline datasets: the glacial regions from Zwally et al. (2012), hereafter ZWA12, and the Ice Sheet Mass Balance Intercomparison Exercise (IMBIE) glacial regions (Rignot et al., 2013), which both cover only the APIS, and the Randolph Glacier Inventory version 7 (RGI Consortium, 2023), covering the peripheral glaciers.

2.4 Grounding line and bed elevations

We used the BedMap3 (Pritchard et al., 2025) vector product of reconciled grounding lines (H. D. Pritchard, June 2025, personal communication). Seafloor and subglacial bed elevations were also extracted from this dataset.

2.5 Firn densification models outputs

To estimate the evolution of the firn air content (FAC) during the period of study and correct the elevation changes obtained from the DEM differencing method, we used outputs from four different firn densification models (FDMs) based on various climate and compaction frameworks.

- The first model, referred to as GSFC-FDM, corresponds to the GSFC-FDMv1.2.1 developed by Medley et al. (2022b). It is based on the Community Firn Model (Stevens et al., 2020) and was forced with Modern-Era Retrospective analysis for Research and Applications, Version 2 (MERRA-2, Gelaro et al., 2017).
- The second model, herafter GEMB-FDM, is the Glacier Energy and Mass Balance (GEMB v1.0, Gardner et al., 2023). It was provided by the NASA Jet Propulsion Laboratory and was forced with ERA5 atmospheric re-analysis model (Soci et al., 2024).
- The third model, IMAU-FDM, was developed at the Institute for Marine and Atmospheric Research Utrecht by Veldhuijsen et al. (2023). It was forced by the Regional Atmospheric Climate MOdel (RACMO2.3p2, van Wessem et al., 2018), which was in turn forced with the ERA5 atmospheric re-analysis model (Soci et al., 2024).

- The fourth model, called MAR-FDM, corresponds to the Modèle Atmosphérique Régional version 3.14 (MAR, Fettweis and Grailet, 2024). It was developed by the Liège University and the Grenoble-Alpes University and was also forced with ERA5 atmospheric re-analysis model (Soci et al., 2024).

2.6 Glacial isostatic adjustment models

We selected three paleoclimatic models to correct the changes related to glacial isostatic adjustment. We use one regional model of Antarctic GIA from Whitehouse et al. (2012) and two global models, ICE-6G_D (VM5a) from Peltier et al. (2015) and Caron et al. (2018). We chose to consider GIA models at both regional and global scale to quantify the uncertainty introduced by differences in solid earth models.

3 METHODS

The complete analysis workflow of this study is summarized in Fig. 3. First, we prepare the DEMs from SPOT5-HRS and REMA and vertically adjust these with laser altimetry data. Then, we compute elevation difference maps. Finally, we convert volume to mass change, taking into account corrections from GIA, firn densification, and ELR models. The detailed steps are described below.

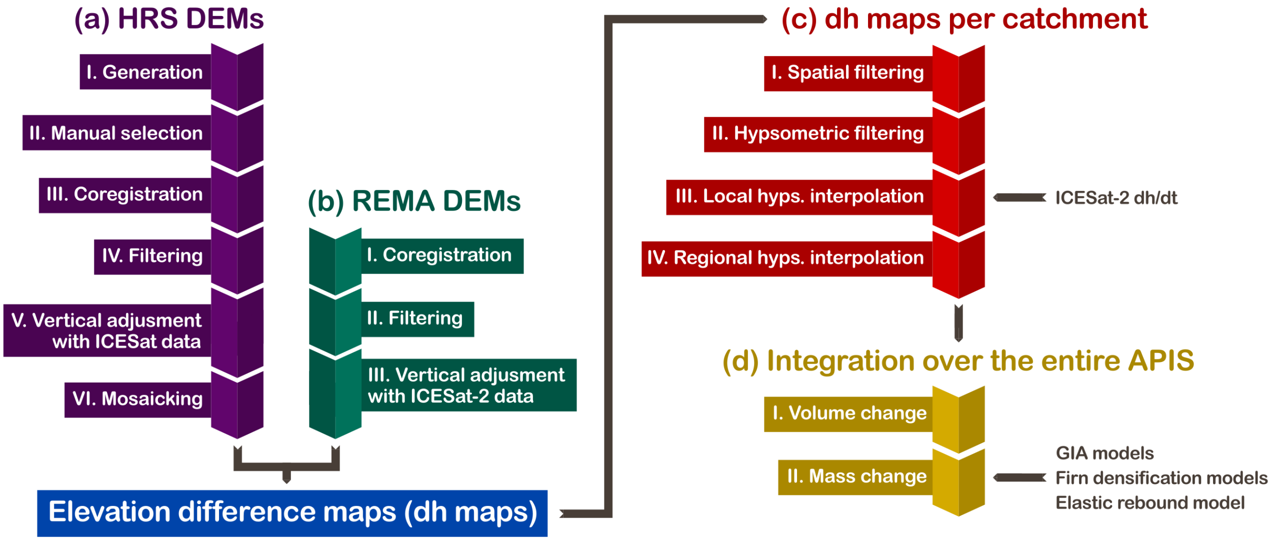

Figure 3. Workflow of the analysis. (a) Processing of the SPOT5-HRS DEMs. (b) Processing of the REMA DEMs. (c) Processing of the elevation difference maps per catchment. (d) Calculations on the entire APIS.

https://doi.org/10.5194/egusphere-2026-729
Preprint. Discussion started: 3 March 2026

3.1 SPOT5-HRS DEM processing

Generation

We used the Ames Stereo Pipeline (ASP, version 3.3.0, Beyer et al., 2018) software developed by NASA to produce DEMs from the optical stereoscopic image pairs. As outlines of the AP vary depending on the dataset considered (up to a few tens of kilometers in at the southern limit with west Antarctica), we used the largest dataset extent, SIL20, to identify the image pairs included in the AP. RPC models were attached to the imagery using *add_spot_rpc* pre-processing routine. We applied the Semi Global Matching algorithm (Hirschmuller, 2008) to correlate the image pairs. We changed the following parameters from the default settings, inspired by Deschamps-Berger et al. (2020):

– stereo-algorithm 1 –xcorr-threshold 1 –corr-kernel 7 7 –corr-tile-size 4096 –ip-per-tile 800 –subpixel-mode 9

We generated DEMs with a pixel size of 20 x 20 m using *point2dem*. Before any further processing, we manually removed the DEMs presenting too few data (less than 20 km^2) or too much noise (from visual inspection). The austral summers of 2006, 2007 and 2008 were selected as they contain the majority of the HRS acquisitions of the AP. We obtained a total of 481 HRS DEMs acquired on 110 different dates between 21 December 2005 and 22 March 2008, which we grouped per austral summer. The temporal coverage is shown in Fig. 2 and spatial coverage in Fig. 1, which contains all geographic information hereafter mentioned. The coverage of each austral summer is available separately in Fig. A1.

Coregistration

All DEMs were coregistered horizontally and vertically to a common reference DEM following Nuth and Kääb (2011) using the Python package $xdem$ (https://zenodo.org/records/11492983). We created the reference DEM by mosaicking the improved TanDEM-X DEM in the northern AP (Dong et al., 2021) with the Copernicus GLO-30 DEM (German Aerospace Center, 2018) edited version of the TanDEM-X DEM in the southern AP. Usually, ice-free terrain of intermediate slope (from 2° to 20°), considered stable, is used to apply the coregistration. However, in the AP, glaciers occupy the vast majority of the surface ($> 99\%$ of the area) and the remaining areas not covered by ice are often small and very steep (Silva et al., 2020). Rock outcrops also become even scarcer in the south of the AP. Therefore, we considered all available elevation data with intermediate slope, including the ice and snow, to perform the coregistration. We identified 20 DEMs with unrealistic horizontal shifts (x- or y-shift larger than $median \pm 3 * NMAD$; normalized median absolute deviation). Three-quarters of these DEMs were successfully re-coregistered with an overlapping HRS DEM, and the remaining ones were kept despite the extreme horizontal shifts, as they provided unique data on flat areas less impacted by a potential coregistration error. We obtained the following mean (μ) and standard deviation (σ) for the x-, y- and z-shifts: μ_x = -0.67 m and σ_x = 12.20 m, μ_y = -24.13 m and σ_y = 12.33 m and μ_z = -3.60 m and σ_z = 5.40 m (Fig. A2).

Filtering

We removed pixels with steep slopes ($\geq$50°) that were likely to have large errors (Toutin et al., 2011). We then computed the elevation difference to the TanDEM-X reference DEM as a first coarse estimate to filter out outliers (threshold of 200 m).

https://doi.org/10.5194/egusphere-2026-729
Preprint. Discussion started: 3 March 2026

Then, an asymmetric filter was added to remove very high positive elevation change values (threshold of +20 m). To remove remaining aberrant pixels, we applied a custom percentile-based radial outlier filter. For each pixel, we calculated the 20th (h_{20}) and 80th (h_{80}) percentile within a disk of a radius (r). Defining a threshold (α), pixels with an elevation h such that $|h - h_{20}| > \alpha$ or $|h - h_{80}| > \alpha$ were removed. We applied three filters with the following parameters: $r = 2$ pixels and $\alpha = 20$ m, $r = 5$ pixels and $\alpha = 50$ m, $r = 10$ pixels and $\alpha = 100$ m. Details on the effects of each filter can be found on Fig. A4. In total, 16% of the initial data were removed.

Vertical adjustment on near-coincident ICESat data

The high vertical accuracy and precision of laser altimetry measurements make them a useful tool for correcting the vertical biases of less accurate DEMs. ICESat elevation measurements have already been used to estimate the accuracy of DEMs (e.g. Howat et al., 2019). Thus, we harnessed the temporal overlap of ICESat and HRS DEMs (Fig. 2) to vertically adjust the latter. The spatial sampling was too sparse to use ICESat elevations for horizontal coregistration, but sufficient for a vertical adjustment.

We preprocessed the GLA12 ICESat data identically to Smith et al. (2020). Then, for each HRS DEM, we selected the closest ICESat campaign in time. This resulted in a 52-day maximum gap between HRS acquisition dates and the central date of ICESat campaigns. We extracted all intersecting points from the chosen campaign. To compute the elevation difference, we bilinearly interpolated the HRS DEM at the coordinates of the ICESat points. We also extracted the slope from the TanDEM-X reference DEM and removed points with a value $\geq 20°$ to mitigate the effect of slope-induced errors. We imposed a minimum of 20 valid points to compute the mean elevation difference and vertically shift the HRS DEMs by the obtained value. 388 of the 481 initial DEMs were corrected. The mean vertical adjustment, added to the z-shift obtained from the coregistration, was 1.30 m with a standard deviation of 3.05 m (Fig. A2).

Due to the wide spacing of the ICESat tracks ($\sim$ 20 to 30 km) and the brief duration of the acquisition campaigns, 93 DEMs had no simultaneous intersecting ICESat points. Two alternative corrections were considered to vertically adjust the DEMs. First, DEMs that overlapped with an ICESat-adjusted neighbor were coregistered to that neighbor (44 DEMs). Then, DEMs with no ICESat-corrected neighbors were coregistered to the REMA DEM mosaic (see Section 3.2), but only using only ice-free terrain with slopes from 2° to 20° (37 DEMs). Any remaining DEMs were removed from the dataset (12 DEMs) with the exception of two DEMs covering the Clarence and Elephant islands (South Shetland Islands archipelago), which were kept uncorrected as they provide unique information on these isolated areas.

Eventually, for each acquisition date, all intersecting HRS DEMs were mosaicked into a single continuous DEM, taking the mean value of overlapping areas. We thus produced 162 mosaics, called HRS segments, covering 76% of the AP surface. The distribution of time differences between the HRS segments acquisition date and the ICESat campaign center date weighted by

https://doi.org/10.5194/egusphere-2026-729
Preprint. Discussion started: 3 March 2026

area has a mean of -4.8 days and a standard deviation of 37.8 days. Given the negligible mean time difference, we infer that potential seasonal errors introduced by this correction are mitigated when analyzing the whole dataset.

3.2 REMA DEMs processing

Selection, masking and coregistration

For each HRS segment, we identified the overlapping REMA DEMs, acquired in the austral summers 2020, 2021 and 2022 (Fig. 2). We limited the day-of-year difference to ± 62 days (2 months) to avoid seasonal errors, except for the particular case of Drygalski and Hektoria-Green-Evans (HGE) glacier system (Fig. 4c and e). Acknowledging that the extreme elevation changes observed in those areas exceed seasonal effects, we extended the day difference to ± 150 and ± 125 days respectively in order to get a more complete coverage.

We used the binary mask associated to each REM DEM to keep only valid pixels i.e. pixels with a 0-flag (no water, nor cloud, nor edge). Then, we coregistered REMA DEMs to the same TanDEM-X reference DEM as the HRS segments (section 3.1)). REMA DEMs with a x- or y-shift outside of the interval $median \pm 3 \cdot NMAD$ were removed. In total, 3 941 DEMs were downloaded, of which 2 796 were successfully coregistered. The x-, y- and z-shifts means (μ) and standard deviations (σ) are the following respectively: $\mu_x = 25.64$ m and $\sigma_x = 15.66$ m, $\mu_y = 6.31$ m and $\sigma_y = 15.44$ m, $\mu_z = -0.43$ m and $\sigma_z = 5.04$ m (Fig. A3).

Vertical adjustment with near-coincident ICESat-2 data

Similarly to the SPOT5-HRS DEMs processing, we vertically adjusted the REMA DEMs using near-coincident laser altimetry data, this time from ICESat-2. For 2 298 REMA DEMs, we extracted intersecting ICESat-2 data acquired ± 31 days apart. We extended the time window to ± 62 days for 227 additional DEMs. All ICESat-2 points with a quality flag equal to 0 and a slope value $\leq 20°$ extracted from the TanDEM-X reference DEM were selected. We set the same threshold of 20 points at minimum as for the SPOT5-HRS DEMs adjustment on ICESat. Then, we bilinearly interpolated the DEMs at each ICESat-2 point and computed the mean elevation difference that was used as a vertical correction. We removed REMA DEMs with a vertical shift larger than 3 NMAD from the median. The mean vertical shift is 0.69 m and the standard deviation is 13.24 m (Fig. A3). We combined all the pre-processed REMA DEMs into a mean mosaic that was used as a stable terrain reference DEM (Section 3.1), covering 90% of the AP surface.

3.3 Elevation difference maps processing

Differencing and filtering

We derived all pairwise elevation difference maps (dh maps) possible between the two elevation datasets SPOT5-HRS and REMA, respecting the maximum 62 day-of-year difference, and obtained 8 381 dh maps. We converted the elevation differences to rates of elevation change (dh/dt maps) by dividing the dh map by the time difference between the two austral summers considered (between 12 to 16 years). To remove remaining aberrant values, we first applied a spatial filter to all the dh/dt maps, inspired by Hugonnet et al. (2021). For each pixel, the 20^{th} (dh/dt_{20}) and 80^{th} (dh/dt_{80}) percentile were calculated within a disk of a radius (r). We set the radius to 5 pixels and the threshold (β) to 0.5 m/a. Pixels with a dh/dt value larger than $dh/dt_{80} + \beta$ or lower than $dh/dt_{20} - \beta$ were excluded. Then, we implemented a filter based on the binning of dh/dt values against elevations extracted from the TanDEM-X reference DEM, independently for each catchment from the SIL20 outlines. The latter is called hypsometric signal and represents the relationship between elevation change rates and elevations at catchment scale. To extract a clear hypsometric signal, we duplicated the dh/dt maps dataset on which we applied a more restrictive spatial filter (radius of 20 pixels and threshold of 1 m/a). For each catchment, we collected all this strictly spatially filtered dh/dt data and distributed it according to 50 m elevation bins. We computed the mean and standard deviation of each bin and defined the filter as $mean \pm 7 * std$. Non-robust statistics were used to account for the effect of valid but outlying values on the metrics, which is essential for further volume calculations. Then, we applied this hypsometric filter on the less strictly spatially filtered dh/dt maps cropped to the catchment outlines. Figure A5 illustrates the effects of the spatial and hypsometric filters on an example catchment. Eventually, we merged all the dh/dt data available for each catchment. In areas with different dh/dt estimations, we used the median value, less sensitive to potentially remaining outliers. The obtained dataset covers 66,7% of the total area of the APIS and is shown on Fig. 4.

Glacier outlines editing

Based on the observation of the elevation difference rates maps here produced and on the BedMap3 grounding line vector product, we manually edited the grounding line (marine terminating glaciers) or terminus (land-terminating glaciers) of 61 catchments from SIL20 outlines. This enabled to more accurately delineate grounded ice before further calculations. We also separated the SIL20 catchments into the peripheral glaciers and the APIS. The two domains defined are very similar to the RGI 7 (peripheral glaciers) and to the IMBIE and ZWA12 outlines (APIS). This, and the fact that the outlines of SIL20 were manually corrected, consolidated our choice of using them as primary outlines.

Interpolation

The HRS segments and REMA DEMs, even if close to providing complete coverage when aggregated (76% and 90% coverage, respectively), do not support a dh/dt dataset covering the entire AP. As complete dh/dt maps are required for further volume and mass changes computations, we included a spatial interpolation step. To add elevation change information where dh/dt map were missing, we extracted elevation data from ICESat-2 matching the same time constraints as for the REMA DEMs extraction (± 62 days apart from the HRS DEM acquisition date) for each HRS segment. We computed the elevation difference rate dh/dt_{IS2} between HRS and ICESat-2. We grouped all the data per catchment and removed pixels outside of $mean \pm 7 * std$.

We then focused on hypsometric methods (McNabb et al., 2019), using first a local hypsometric method to fill the uncovered areas. For each catchment, we calculated again the hypsometric signal per 50-m elevation bins. To do so, we averaged the hypsometric signals coming from: 1. the dh/dt maps between REMA and HRS DEMs, 2. the dh/dt_{IS2} points between HRS DEMs and ICESat-2 data. We extracted the elevation of empty pixels from the TanDEM-X reference DEM used previously.

https://doi.org/10.5194/egusphere-2026-729
Preprint. Discussion started: 3 March 2026

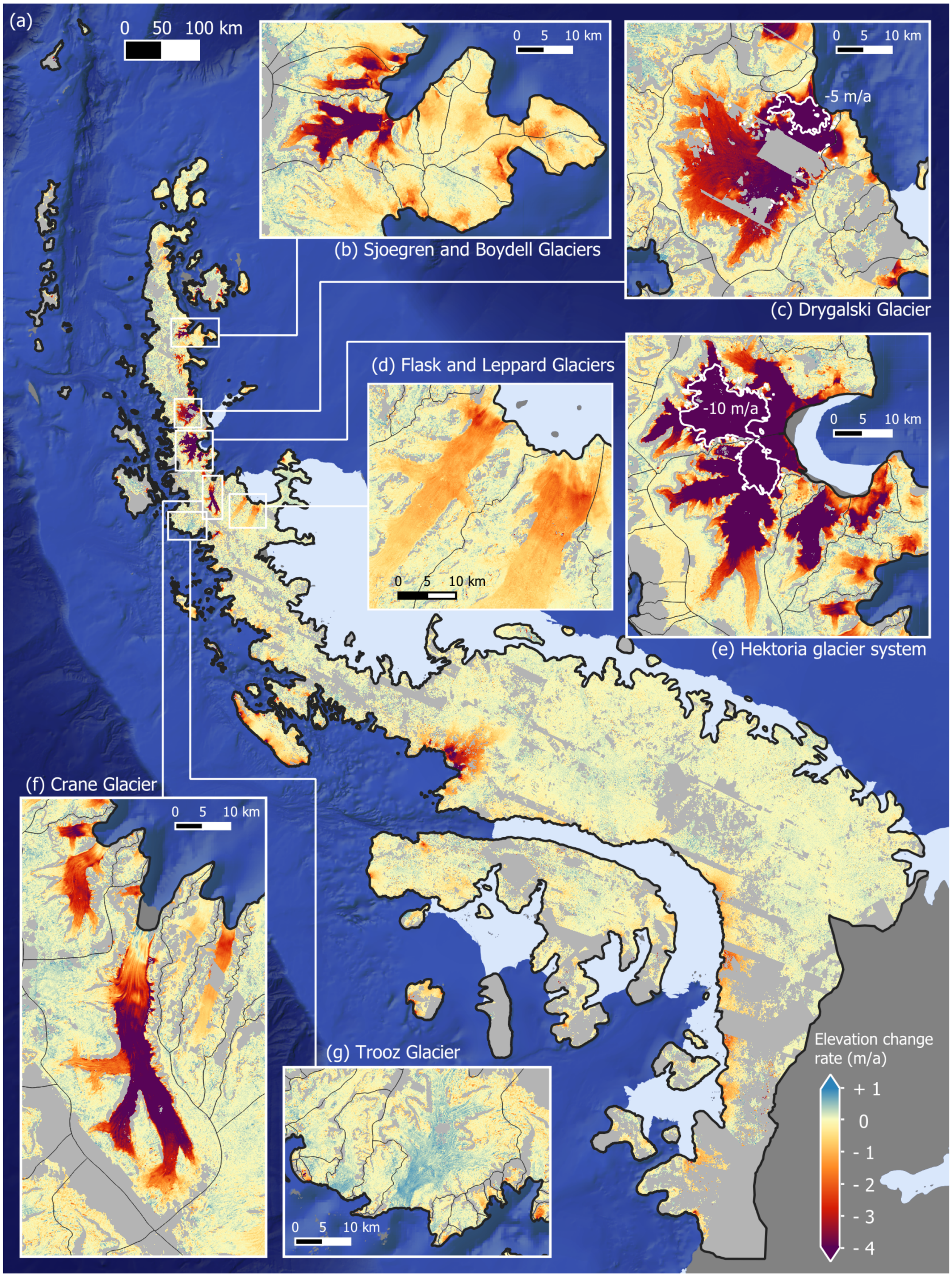

Figure 4. Elevation change rates over the Antarctic Peninsula between 2007 and 2021. Five catchments are highlighted in the insets (b) to (f), with SIL20 catchment outlines plotted in thin black lines. On (c) and (e), the white line indicates the -5 m/a and -10 m/a delimitation. The background oceanic hillshade and the ice shelves outlines come from BedMap3 (Pritchard et al., 2025).

Eventually, we considered the mean dh/dt value of the corresponding elevation bin to fill the missing data. For 30 catchments representing 3% of the total study area, no dh/dt data was available. We applied a regional hypsometric method to estimate the elevation change on those catchments: we extracted an AP-scale hypsometric signal considering all dh/dt data available that was used to fill the last voids (see Fig. 5a).

3.4 Volume and mass changes

To obtain rates of elevation change that reflect glacier evolution, several corrections have to be applied. As commonly done in ice sheet mass changes studies (e.g. Smith et al., 2020, Sanchez Lofficial et al., 2025), we considered the three following corrections: firn density changes (dh_{FAC}/dt), glacial isostatic adjustment (dh_{GIA}/dt) and the elastic rebound (dh_{ELR}/dt). These corrections are summarized into equation 1, where dh/dt represents the elevation difference rates obtained from the initial dh/dt maps and dh_{ice}/dt corresponds to the corrected elevation difference rates. The latter directly reflects ice changes and can be expressed in meters of ice per year (m_{ice}/a).

$$dh_{ice}/dt = dh/dt - dh_{FAC}/dt - dh_{GIA}/dt - dh_{ELR}/dt \tag{1}$$

First, we corrected elevation changes related to the evolution of the firn density. A common variable used to characterize it is the firn air content (FAC). The spatial and temporal evolution of the FAC can be modeled thanks to firn densification models (FDMs). However, large discrepancies exist between the FDMs employed, within the scheme, the climatic forcing and the results produced (Sanchez Lofficial et al., 2025). Therefore, we used the outputs of 4 different FDMs (section 2.5): GSFC-FDM, GEMB-FDM, IMAU-FDM, MAR-FDM. For each of them, we extracted the mean FAC over the three austral summers for the two epochs of study and computed the difference to obtain the FAC change dh_{FAC}/dt over 2007−2021. We spatially extrapolated the dh_{FAC}/dt maps on areas with missing data (Fig. A6). Then, we removed the effect of the glacial isostatic adjustment using three GIA models (section 2.6). As for the FAC correction, we computed the elevation change independently for each GIA model before averaging (Fig. A7). Eventually, we estimated the elastic rebound from the solid Earth caused by current ice changes using the LoadDef code developed by Martens et al. (2019). We used the corrected mass changes (without the elastic correction) with a spatial resolution of 900 m as the input load map and set the parameters to the default settings. More precisely, we kept the Preliminary reference Earth model from Dziewonski and Anderson (1981), commonly used as a reference for solid earth parameters in geodesy studies.

Figure 5 shows dh/dt maps including the uncorrected elevation change and the applied corrections. To calculate volume changes, we integrated the elevation change rates over the areas defined by the four outline datasets used in the study (SIL20; ZWA12; IMBIE and RGI7, see section 2.3). To calculate mass change, we multiplied the corrected volume changes by ice density (917 kg/m^3), as they reflect ice changes.

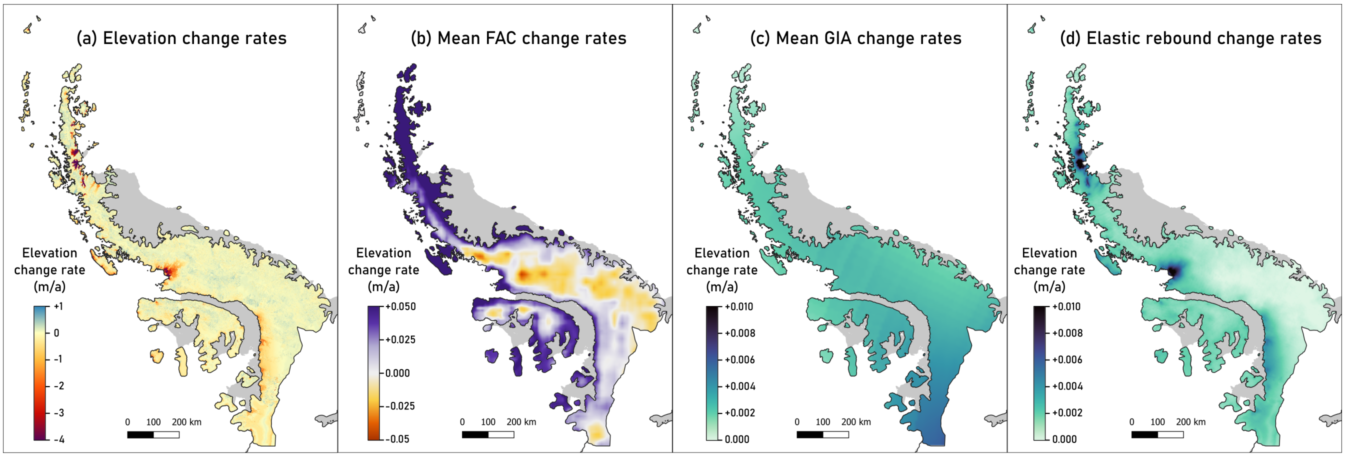

Figure 5. Complete elevation change rates map and the elevation corrections applied, (2007−2021). (a) Interpolated elevation change rates map, (b) Mean FAC changes obtained from the four firn densification models, (c) Mean GIA changes calculated from the three GIA models, (d) Solid earth elastic rebound changes computed with LoadDef. The GIA correction is the only one that is not specific to the period 2007−2021. SIL20 outlines are indicated in black and ice shelves (Pritchard et al., 2025) in grey.

3.5 Uncertainty quantification

To estimate the volume change uncertainty, we considered several sources of uncertainty, assumed independent, summarized in Equation 2. We consider that the uncertainties related to the area and the ELR are negligible in comparison to other sources. $\sigma_{\overline{dh}_{FAC}/dt}$ and $\sigma_{\overline{dh}_{GIA}/dt}$ represent the elevation change rate uncertainty induced by the corresponding corrections. Separating the elevation change rates into the observed elevation change rates dh_{obs}/dt and the interpolated elevation change rates dh_{interp}/dt, we define two distinct associated uncertainties, $\sigma_{\overline{dh}_{obs}/dt}$ and $\sigma_{\overline{dh}_{interp}/dt}$. A_{tot} and A_{obs} correspond to the total area and the area covered with dh_{obs}/dt maps, respectively.

$$
\begin{aligned}
\sigma^2_{dV_{ice}/dt} &= (\sigma^2_{dV_{obs}/dt} + \sigma^2_{dV_{interp}/dt}) + \sigma^2_{dV_{FAC}/dt} + \sigma^2_{dV_{GIA}/dt} \\
&= A^2_{obs} \cdot \sigma^2_{dh_{obs}/dt} + (A_{tot} - A_{obs})^2 \cdot \sigma^2_{dh_{interp}/dt} + A^2_{tot} \cdot (\sigma^2_{dh_{GIA}/dt} + \sigma^2_{dh_{FAC}/dt})
\end{aligned}
\qquad (2)
$$

Ultimately, we estimate the mass changes uncertainty as $\sigma^2_{dM/dt} = \rho_{ice} \cdot \sigma^2_{dV_{ice}/dt}$, with ρ_{ice} = 917 kg/m^3.

To quantify the uncertainty of the observed elevation changes $\sigma_{\overline{dh}/dt_{obs}}$, we applied the method of Hugonnet et al. (2022) that models and propagates autocorrelated elevation change errors. We used the difference between coincident DEMs as an error proxy, instead of the commonly-used differences over static surfaces that can rely on acquisitions of any date, due to the lack of such static surfaces on the AP. Two DEMs acquired within close dates should have near zero elevation changes, thus their elevation difference is a common proxy for errors. We identified multiple coincident pairs of HRS DEMs (13) or REMA DEMs (23), acquired up to five days apart and with a common area of at least 1 km^2. Then, we computed the standard deviation

https://doi.org/10.5194/egusphere-2026-729
Preprint. Discussion started: 3 March 2026

of the elevation difference for all HRS and REMA pairs, as a measure of the per-pixel random error of each sensor, $\sigma_{dh_{HRS}}$ and $\sigma_{dh_{REMA}}$ respectively. Those values account twice for the error as pairs of DEMs are considered, so we divided them by $\sqrt{2}$ before further calculations. To derive the average per-pixel random error of the dh maps between HRS and REMA DEMs, we combine the two errors previously calculated considering them independent, such that $\sigma^2_{dh_{obs}} = \sigma^2_{dh_{HRS}} + \sigma^2_{dh_{REMA}}$. We obtained the following values: $\sigma_{dh_{HRS}} = 3.92$ m, $\sigma_{dh_{REMA}} = 4.06$ m and $\sigma_{dh_{obs}} = 5.64$ m.

To constrain the autocorrelation of elevation errors, we derived empirical variograms of the elevation differences of the coincident DEMs from Dowd's median estimator (Dowd, 1984) using the Python package $xdem$. These variograms, which describe the correlation of errors between two points as a function of their distance, were averaged to get a mean variogram representing each sensor, HRS and REMA. We then modeled the two mean empirical variograms as the sum of two Gaussian and a spherical function (Fig. A8 and A9) to represent the nested autocorrelation structure often observed in elevation data and critical to robust error propagation for volume changes (Rolstad et al., 2009; Hugonnet et al., 2022). HRS elevation errors were correlated by 100%-20% until 100 m, then by 20%-5% until 200 m, then by less than 5% until 5 km. REMA elevation errors were correlated by 90-10% until 100 m, then by 10%-5% until 200 m, then by less than 5% until 2 km. We then used the above models to propagate uncertainties spatially from pixel to area into uncertainties of the mean elevation change $\sigma_{\overline{dh}_{obs}}$ over a defined area. To this end, we derived the numbers of effective samples $N_{eff_{HRS}}$ and $N_{eff_{REMA}}$ from the two variogram models following Hugonnet et al. (2022). We propagated the uncertainties coming from the two sensors as $\sigma^2_{\overline{dh}_{obs}} = \sigma^2_{dh_{HRS}}/N_{eff_{HRS}} + \sigma^2_{dh_{REMA}}/N_{eff_{REMA}}$. Ultimately, $\sigma_{dh_{obs}}$ was divided by the period of study (14 years) to obtain $\sigma_{\overline{dh}_{obs}/dt}$.

Then, we applied a leave-block-out cross-validation method (e.g. Le Rest et al., 2014; Roberts et al., 2017) to estimate the uncertainties that arise from the interpolation, annotated $\sigma_{\overline{dh}_{interp}/dt}$. We considered the 709 catchments from the SIL20 outlines with a dh_{obs}/dt coverage larger than 80% (44% of the AP surface). For each of them, we created artificial gaps that were then filled following the same methodology as in the data processing, i.e. using the local hypsometric interpolation when possible, and otherwise the regional hypsometric interpolation. To create gaps, we isolated elevation bands of different widths and central elevations, determined from the TanDEM-X reference DEM, on the dh_{obs}/dt map. First, this enabled to better reproduce the shape of our existing data gaps than removing pixels at random coordinates. Second, by varying the width and the central elevation of the hypsometric band removed, we created data gaps ranging from 0 to 100%. For each artificial gap generated, we then derived the mean of the difference between interpolated and initial dh_{obs}/dt, which served as an error proxy for our spatially-integrated elevation differences over interpolated areas.

We grouped all the means obtained by percent of missing data and, from their distribution, derived the mean and a robust dispersion metric, (84^{th} percentile - 16^{th} percentile)/2. The mean accounts for a possible bias introduced by the interpolation, whereas the robust dispersion metric represents the spread around the mean value generated by the interpolation. We modeled the mean with a piecewise-defined affine function, first constant to 0 until 40% of gaps, then linear reaching the value of

0.06 m/a at 100% of gaps and we fitted a 3-degree polynomial curve to the series of robust dispersion metrics obtained (Fig. A10). The sum of the mean of the mean and the robust dispersion metric of the mean was then used to estimate the interpolation uncertainty. In other words, given a gap percentage over a catchment, we extracted the corresponding uncertainty $\sigma_{\overline{dh}_{interp}/dt}$ from the modeled curves.

Finally, we estimated the uncertainties of the FAC ($\sigma_{\overline{dh}_{FAC}/dt}$) and GIA ($\sigma_{\overline{dh}_{GIA}/dt}$) corrections based on the standard deviation between the elevation changes obtained with the different models. We assume conservatively that these uncertainties are fully correlated at the scale of the AP, and thus use this value at every scale (pixel, catchment, whole region). Regarding the elevation change rate uncertainties, we consider $\sigma_{\overline{dh}_{interp}/dt}$ fully correlated and apply the method described above to the entire AP, and $\sigma_{\overline{dh}_{obs}/dt}$ fully independent (see Fig. A8 and A9). Uncertainties are then reported as ±2-σ (95% confidence interval).

4 RESULTS

Antarctic Peninsula

In Table 1, we report our mass change estimates for the period 2007−2021, calculated over several regions defined by different outlines data sets listed in section 2.3. Over the similar ZWA12 and IMBIE outlines, we obtain mass changes of -26.5 ± 5.3 Gt/a and -26.9 ± 5.3 Gt/a. For the peripheral glaciers, whose outlines are in the RGI 7 database, we obtained mass changes of -13.8 ± 2.7 Gt/a. Finally, using the SIL20 outlines that include both the ice sheet and the peripheral glaciers with an updated grounding line, we derived a total mass change of -41.9 ± 8.5 Gt/a, equivalent to a sea-level contribution of 0.12 ± 0.02 mm/a (2.8% of the 2007−2021 sea-level rise calculated from the Aviso product).

Outlines	Area ($\mathrm{km^2}$)	$\mathrm{dM/dT}$ ($\mathrm{Gt\ a^{-1}}$)	$\mathrm{dM_{FAC}/dT}$ ($\mathrm{Gt\ a^{-1}}$)	$\mathrm{dM_{GIA}/dT}$ ($\mathrm{Gt\ a^{-1}}$)	$\mathrm{dM_{ELR}/dT}$ ($\mathrm{Gt\ a^{-1}}$)	$\mathrm{dh_{ice}/dT}$ ($\mathrm{m_{ice}\ a^{-1}}$)
SIL20	335 314	-41.9 ± 8.5	3.0 ± 6.2	0.7 ± 0.8	0.3	-0.12 ± 0.02
SIL20 (APIS)	253 037	-28.2 ± 5.9	1.5 ± 4.5	0.6 ± 0.7	0.2	-0.11 ± 0.02
SIL20 (periphery)	82 277	-13.7 ± 2.8	1.5 ± 1.8	0.1 ± 0.1	0.1	-0.16 ± 0.03
IMBIE	230 294	-26.9 ± 5.3	1.9 ± 4.4	0.5 ± 0.6	0.3	-0.11 ± 0.01
ZWA12	226 448	-26.5 ± 5.3	1.9 ± 4.3	0.5 ± 0.6	0.3	-0.11 ± 0.01
RGI v7	79 703	-13.8 ± 2.7	1.6 ± 1.8	0.1 ± 0.1	0.1	-0.16 ± 0.03

Table 1. Mass and ice elevation changes for the four outline datasets over the period 2007−2021. For each outline dataset, the following variables are indicated: the area encompassed, the total mass changes (dM/dT), the mass changes from the GIA, FAC and ELR corrections (dM_{FAC}/dT, dM_{GIA}/dT and dM_{ELR}/dT respectively) and the ice elevation changes (dh_{ice}/dT). SIL20 catchments were divided into APIS outlet glaciers and peripheral glaciers.

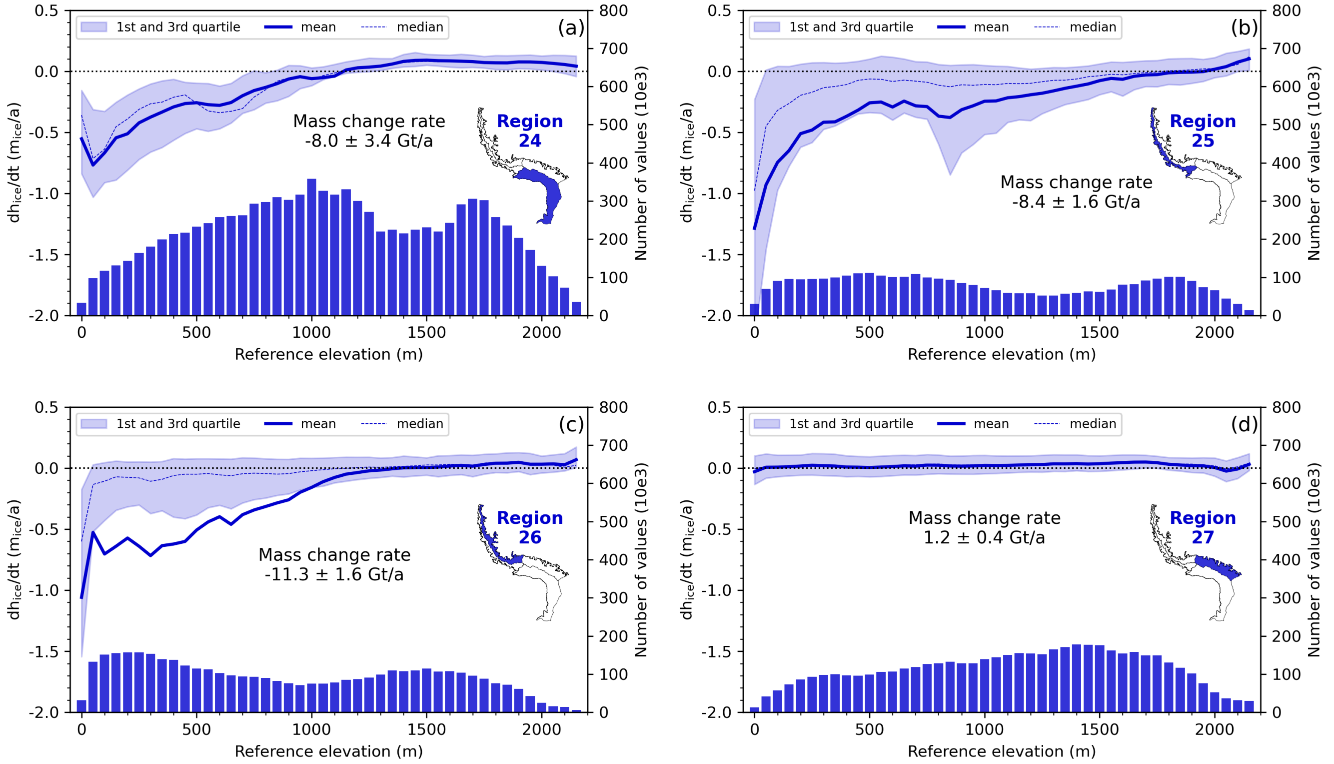

Figure 6. Hypsometric signal of ice elevation changes over AP main regions. For each region from the ZWA12 outline (a)-(d), the histogram at the bottom shows the distribution of elevations over the region. The distribution (median, mean, 1^{st} and 3^{rd} quartiles) of ice elevation change rates per elevation bin are plotted at the top.

Despite rapidly thinning grounded outlet glacier tongues, wide portions of the AP are close to balance (Fig. 4 and Fig. 5a). This is especially noteworthy on the high-altitude center plateau as well as for various locations along the coast (e.g. Larsen C, Wilkins Coast). Mass losses are concentrated in a small number of glaciers that exhibit intense thinning. Most of them are located in the northeastern part (Larsen A & B Embayments, Larsen Inlet), in the mid-southern part (Wordie Bay and along the George VI Ice Shelf) and on the peripheral islands (e.g. Adelaide, Liard, James Ross Islands). Several areas also present coherent thickening patterns, including the northwest of the APIS (Davis Coast), parts of the Jason Peninsula in the northeast and along the Black and Lassister Coasts in the southeastern part.

Regional scale

Patterns of ice elevation changes differ from region to region. To identify regional differences in the ice elevation changes, we used the four regions from the ZWA12 outline to estimate the dh_{ice}/dt hypsometric signal of each of them. The results obtained are presented in Fig. 6, revealing large differences between the regions. For all of them however, mass loss is concentrated at elevations below 800 m. The largest contrast between low and high elevations is found in Region 24 (Fig. 6a), vastest of all regions. Here, the elevation change dh_{ice}/dt shifts from very negative values at low elevation, to significantly positive values above 1 200 m. The most negative dh_{ice}/dt values are found between 50 m and 150 m and reach -0.72 m$_{ice}$/a on average. Below 50 m, the scarce zones are dominated by less negative dh_{ice}/dt signal.

Regions 25 and 26 (Fig. 6b and c) show similar dh_{ice}/dt signals and elevation distributions. In both cases, elevations follow a two-peak distribution, one at low elevations (0 m − 600 m) and another at high elevations (1 500 m − 2 000 m). Contrary to Region 24, the most negative dh_{ice}/dt signal is observed in the lowest elevation bin (0 m − 50 m), reaching a mean of -1.29 m$_{ice}$/a in Region 25 and -1.06 m$_{ice}$/a in Region 26. The dh_{ice}/dt signal then gradually increases towards a close-to-zero elevation change rate at the highest elevations. For these two regions, a few glaciers at low elevations have a thickening signal which dominates the third quartile range. For example, between 0 m and 800 m, Trooz Glacier (Region 25, Fig. 4g) presents a mean ± 2-σ ice elevation change rate of +0.32 ± 0.26 m$_{ice}$/a. In Region 25, the negative peak of the dh_{ice}/dt first quartile between 800 m and 1 000 m is caused by ice-dynamical mass loss of Fleming Glacier. Similarly, the very negative signal at low elevations is largely due to this glacier. In Region 26, the large difference between the mean and the median dh_{ice}/dt below 1 200 m of elevation reveals the presence of extremely negative dh_{ice}/dt values that bring down the mean to -1.06 m$_{ice}$/a. Indeed, this region includes the majority of the rapidly thinning glaciers, which reach local minimum elevation change rates of -17.21 m$_{ice}$/a at Hektoria Glacier, -14.25 m$_{ice}$/a at Drygalski Glacier, and -6.63 m$_{ice}$/a at Crane Glacier. Region 27 (Fig. 6d) contains a large area at high elevations, and has a slightly positive mass changes of 1.2 ± 0.4 Gt/a. This mass gain arises from positive dh_{ice}/dt signals observed at all elevations over the region. The amplitude between the first and third quartiles is particularly limited and remains below 0.32 m$_{ice}$/a. It is the only region exhibiting statistically significant mass gain over the study period.

We used the division of SIL20 catchments into peripheral glaciers and APIS catchments to document differences between the two domains. The mean dh_{ice}/dt of peripheral glaciers is -0.16 ± 0.03 m$_{ice}$/a, significantly more negative than the rate of -0.11 ± 0.02 m$_{ice}$/a for APIS (see Table 1). The peripheral glaciers contain more areas at low elevations (between 0 m and 500 m), which correspond to the elevations with the most negative dh_{ice}/dt signal (Fig. A11). Thus, if APIS catchments represent 75% of the total area, they account for -28.2 ± 5.9 Gt/a, i.e. 67% of the total mass loss, whereas peripheral glaciers, covering 25%, account for -13.7 ± 2.8 Gt/a, i.e. 33% of the total mass loss.

Glacier scale

The mean ice elevation change rate for selected catchments from the SIL20 outline dataset is shown in Fig. 7. It highlights the diversity of ice elevation change patterns at a very local scale (< 10 km). Adjacent catchments can present opposite changes, such as Stefan Ice Piedmont (-0.85 ± 0.12 m$_{ice}$/a) and Peter Glacier (+0.18 ± 0.10 m$_{ice}$/a). The Jason Peninsula presents a clear thickening pattern (e.g. G298518E66143S Glacier : +0.20 ± 0.08 m$_{ice}$/a) while its northern tip exhibits dh_{ice}/dt as negative as -0.78 ± 0.10 m$_{ice}$/a. The east-west gradient in the north of the AP is also clearly visible, with very negative mean dh_{ice}/dt in the Larsen A & B Embayments, Larsen Inlet and Prince Gustav Chanel (east) facing close to equilibrium catch-

https://doi.org/10.5194/egusphere-2026-729
Preprint. Discussion started: 3 March 2026

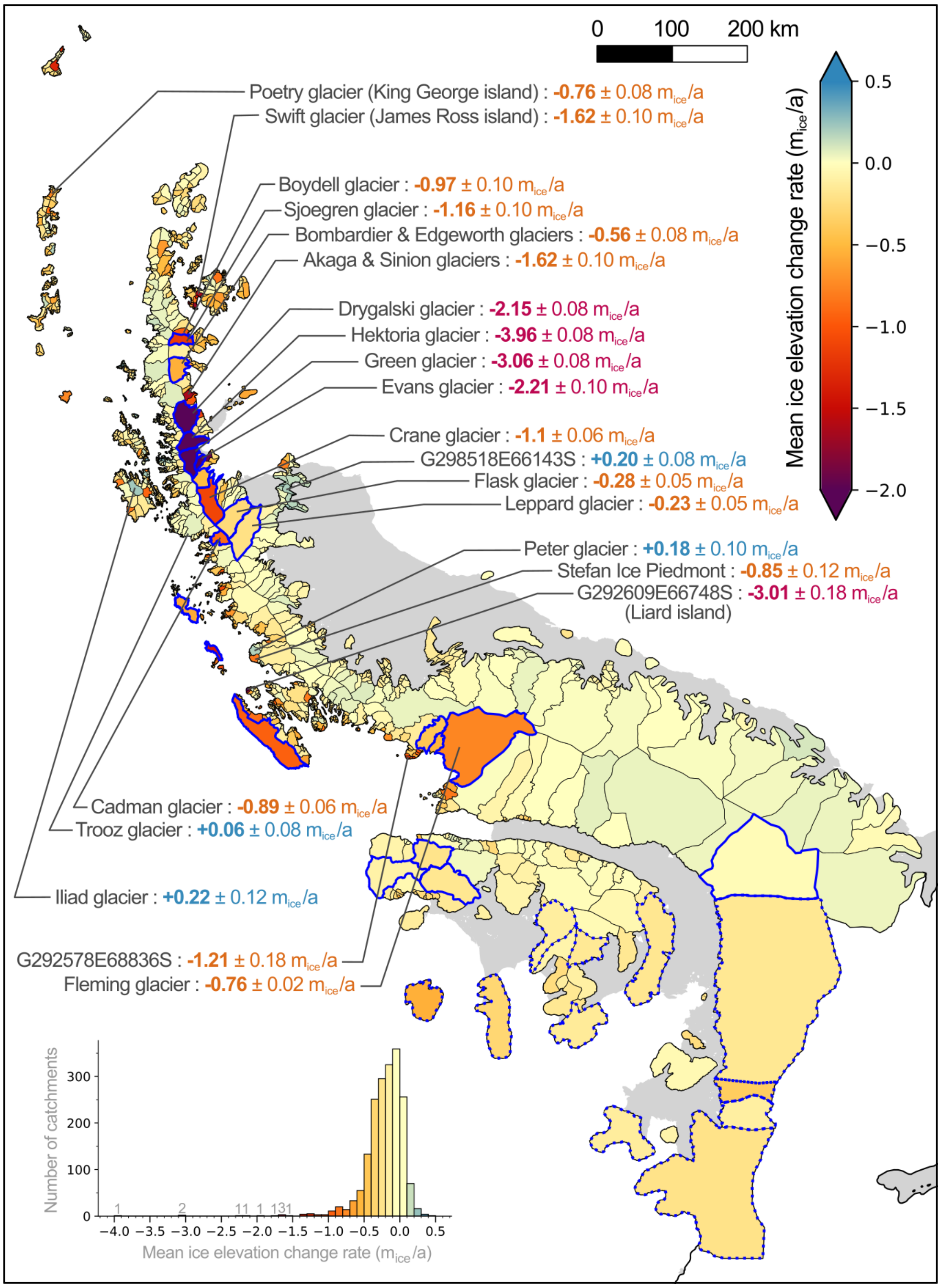

Figure 7. Mean ice elevation change rate of AP glaciers, 2007−2021. The value of the mean ice elevation change rate of 22 catchments is highlighted. Positive mean ice elevation change rates are indicated in blue, negative until -2.00 m/a in orange and below in magenta. SIL20 catchment outlines are indicated in black and ice shelves (Pritchard et al., 2025) in grey. The distribution of mean dt_{ice}/dt is shown in the bottom left corner. The number of catchments is indicated above each column if it is less than three. The 31 catchments presenting the highest mass losses are outlined in blue, with a continuous (≥60% data coverage) or dashed (<60% data coverage) line.

https://doi.org/10.5194/egusphere-2026-729
Preprint. Discussion started: 3 March 2026

ments along the Danco and Davis Coasts (west). Thanks to the high spatial resolution of the dh_{ice}/dt maps, small glaciers (e.g. G292609E66748S (Liard island), 15 km^2, and G292578E68836S, 21 km^2, see Fig. 7) can be observed and analyzed, including local spatial patterns inside the catchment.

A small number of glaciers accounts for the majority of the AP mass changes. Of all catchments, 24 show a significant (2-σ) thickening signal. They cover 21% of the total area, and account for a mass gain of 3.0 ± 0.5 Gt/a. To the contrary, 338 catchments show a significant (2-σ) negative mean dh_{ice}/dt. They cover 42% of the AP and correspond to a mass loss of -38.6 ± 2.4 Gt/a. The remaining 1 507 catchments, that do not present a significantly positive or negative ice elevation change rate, cover 37% of the AP total area, representing a mass change of -6.2 ± 2.8 Gt/a. Considering the cumulative series of mass changes, we observe that 31 catchments, outlined on Fig. 7, generate 80% of the total mass loss (-33.6 ±6.0 Gt/a). They range between -5.39 ± 2.2 Gt/a (G289555E73912S, feeding the southern part of Georges VI Ice Shelf) and -0.2 ± 0.04 Gt/a (Jorum Glacier). The spatial distribution of these major contributors highlights the predominance in terms of mass losses of the northeastern part of the AP (Sjoegren, Bombardier-Edgeworth, Drygalski, Hektoria, Evans, Jorum, Crane, Flask and Leppard Glaciers, from north to south). It also emphasizes the importance of taking into account the peripheral glaciers. Adelaide, Lavoisier and Renaud Islands are listed among the 31 catchments losing most mass, as well as several catchments from Alexander Island.

5 DISCUSSION

5.1 Spatial patterns and spatial variability

Comparison to other studies

We compared our dh/dt maps to those from previous studies, on the APIS (Fig. 8) and on the peripheral glaciers (Fig. 9), selecting the closest time period available when possible. These studies are based on different acquisition techniques, thus presenting different coverages, noise and spatial resolutions. They also cover different time periods, which durations range between 4 to 15 years. This spatial comparison highlights the differences and similarities between the studies but also the advantages and drawbacks of each technique.

Focusing on the APIS (Fig. 8), we compared our results to the three following studies: Seehaus et al. (2023) (Synthetic Aperture Radar or SAR), Smith et al. (2020) (laser altimetry) and Scambos et al. (2014) (optical stereoscopic imagery). Over the APIS, the glaciers presenting extreme thinning rates, such as Drygalski Glacier and HGE glacier system, are clearly visible in all studies (Fig. 8a−d). Similarly, the spatial pattern of intense thinning of a large part of the Fleming Glacier and slight thickening in the upper part of the catchment is observed by all three studies that cover it (Fig. 8e−g). However, many differences in the observed patterns arise, underlying the difficulties inherent in each method. First, the level of noise is higher in the two studies covering a short period ($\leq$ 5 years), Seehaus et al. (2023) and Scambos et al. (2014). Our study benefits from the long time period of study (14 years), which enables us to largely reduce the noise, especially in the close-to-balance areas.

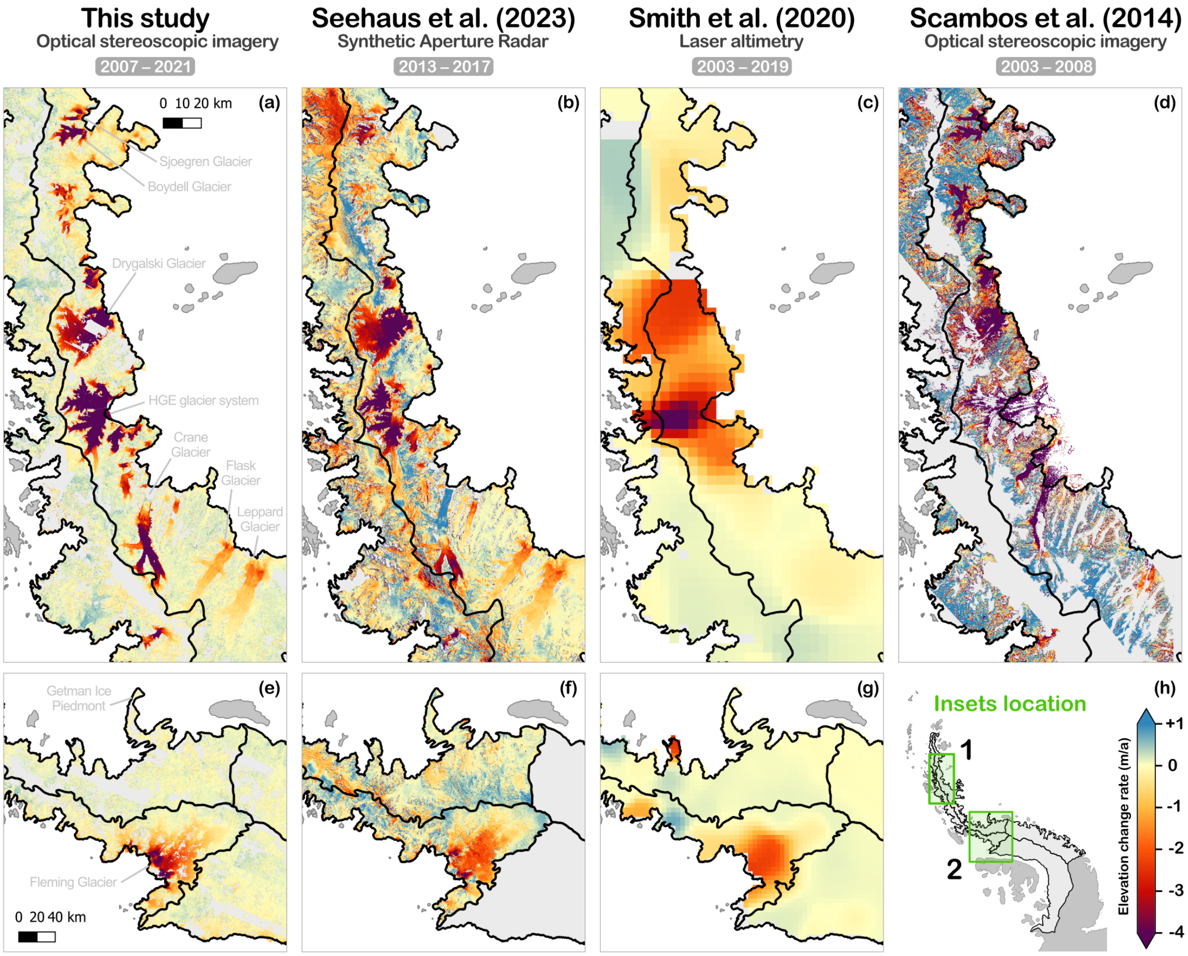

Figure 8. Spatial comparison of elevation change rates maps on selected regions of the APIS. The results from four different studies (this study, Seehaus et al. (2023), Smith et al. (2020) and Scambos et al. (2014)) are compared over two different sites, on panel (a)−(d) and (e)−(g) respectively. The location of the sites is indicated on the last panel (h). The same color scale is used for all maps, but the spatial scale is different for the two sites. The ZWA12 outlines are plotted in black. Note that the elevation change rates map from Scambos et al. (2014) covers only the northern APIS, which does not include the second site of comparison. Note also the different time periods.

Then, regarding the laser altimetry study (Smith et al., 2020), the 5-km resolution added to the interpolation required to obtain gridded data leads to very smooth maps. A consequence is that the mass loss is not well localized, with negative dh/dt values leaking outside the high-loss glacier catchments. Next, Seehaus et al. (2023) and Smith et al. (2020) both provide a complete dh/dt coverage of the APIS. In contrast, the datasets from our study and Scambos et al. (2014) present numerous data gaps that required interpolation methods. Eventually, the dh/dt dataset based on Synthetic Aperture Radar measurements (Seehaus et al., 2023) presents many unrealistic patterns such as the intense thinning at the highest elevations of the western outlet glaciers at the latitude of Boydell and Sjoegren Glaciers, not observed by the other studies (Fig. 8b). This is likely linked to the complex correction of firn penetration biases, exacerbated by the short period of study. Scambos et al. (2014) dt/dt maps seem to include a systematic bias in high elevation areas (Fig. 8d), which is hard to correct because of the scarce stable areas in the region.

Over the peripheral glaciers (Fig. 9), this study was compared to three other dh/dt datasets: Hassan et al. (2025) (laser altimetry), Jakob and Gourmelen (2023) (swath interferometric radar altimetry) and Hugonnet et al. (2021) (optical stereoscopic imagery). As on the APIS, the four studies agree on the spatial changes of several areas, such as the negative signal over the Snow hill Island (Fig. 9a−d), the thinning of Hampton Glacier on Alexander Island and the thickening over the western coast of the Rothschild Island (Fig. 9i−l). The thinning outlet glaciers from James Ross Island are identified by all studies except the laser altimetry one (Hassan et al., 2025), likely a result of its too coarse resolution. Hugonnet et al. (2021) and Jakob and Gourmelen (2023) are affected by a high level of noise, mostly on the high elevation areas and at the coast, respectively. The central part of the Alexander Island tip is problematic for all four studies, in terms of interpolation artifacts, missing data and noise. Both Hassan et al. (2025) and Hugonnet et al. (2021) provide nearly complete maps, whereas our study and Jakob and Gourmelen (2023) present large missing areas, in particular at the central parts of the islands. The peripheral glaciers, through their reduced size in comparison to the APIS, challenge the capabilities of each measurement technique.

Complementarity between altimetry and optical stereoscopy

The spatial comparison detailed previously also emphasizes the complementarity between the methods, in particular between the laser altimetry and the optical stereoscopic imagery, which both capture surface elevations without firn penetration biases. Satellite laser altimetry measurements, following orbital tracks of variable spacing, require interpolation methods to obtain smooth dh/dt maps at a spatial resolution of $1-5$ km. Over wide homogeneous areas, e.g., the ice sheet areas outside of the northern APIS, this is very suitable and the high vertical accuracy allows one to precisely measure small elevation changes. This is exactly where optical stereoscopic methods can struggle, producing many artifacts, outliers or simply data gaps. However, intense small-scale dh/dt signals can be missed by sparse laser altimetry measurements. On Fig. 8, the strongly negative dh/dt signal from Sjoegren and Boydell Glaciers is present in the three high-resolution datasets (this study, 30 m; Seehaus et al. (2023), 30 m, Scambos et al. (2014), 50 m), but not in the 5-km one (Smith et al., 2020). Likewise, the localized thinning of Crane, Flask and Leppard Glaciers is completely absent from this dataset. Additionally, when the signal is sufficiently wide to be observed by laser altimetry, the elevation change measurements are still lower (in absolute value) than those observed by high-resolution methods. For example, the HGE glacier system elevation change signal is less negative and more spread out

https://doi.org/10.5194/egusphere-2026-729
Preprint. Discussion started: 3 March 2026

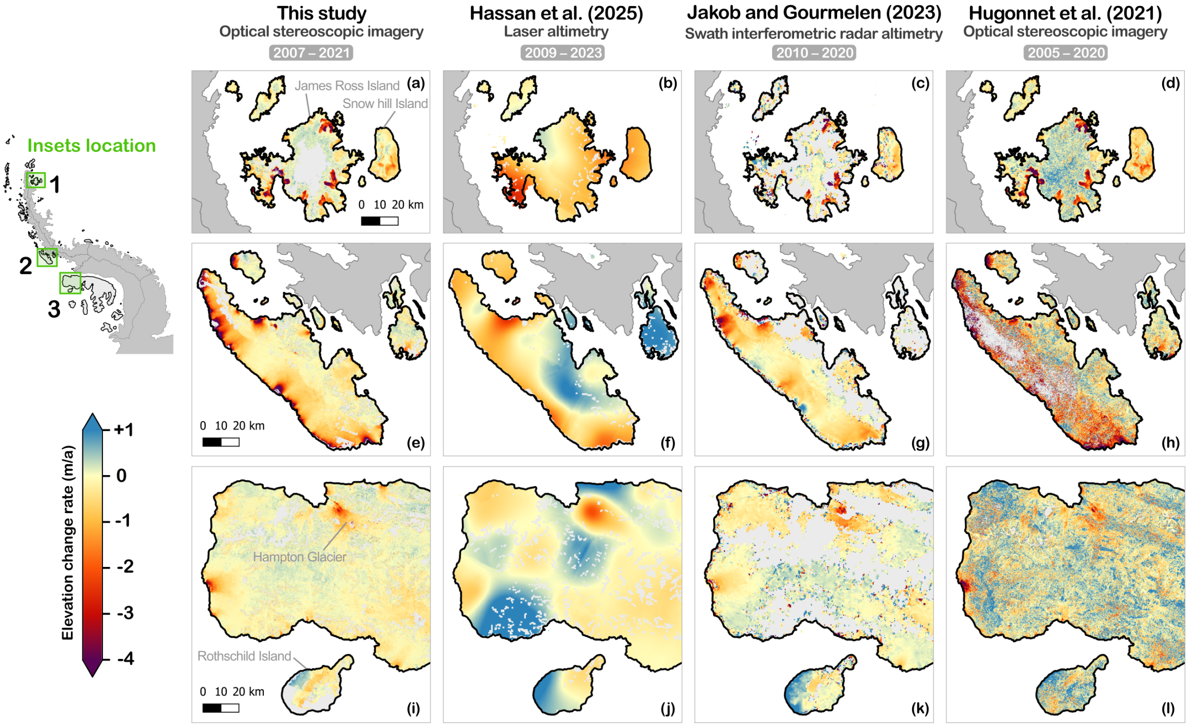

Figure 9. Spatial comparison of elevation change rates maps on selected peripheral glaciers. The results from four different studies (this study, Hassan et al. (2025), Jakob and Gourmelen (2023) and Hugonnet et al. (2021)) are compared over three different sites, on panel (a)−(d) for Vega, James Ross and Snow hill Islands, (e)−(h) for Adelaide Island and (i)−(l) for Alexander Island, respectively. The location of the sites is indicated on the left side. The same color scale is used for all maps and the spatial scale is identical for the three sites. The outlines from RGI Consortium (2023) are plotted in black.

on Fig. 8b than on the other panels a, c and d. Furthermore, the laser altimetry can be very sensitive to outliers that sometimes propagate, as around the Getman Ice Piedmont Glacier (Fig. 8g) or on Alexander Island (Fig. 9j). On the other side, optical stereoscopy allows the observation of very local changes at high spatial resolution. Still, it requires costly data processing and storage, and remains less efficient than laser altimetry on homogeneous areas, in terms of data gaps and vertical accuracy. This illustrates the potential of combining optical stereoscopic dh/dt maps and laser altimetry to observe ice sheet and glacier elevation change at small scale as well as over wide homogeneous areas.

5.2 Mass changes of the AP

We extracted the APIS mass changes for the three ice sheet observation methods from the Otosaka et al. (2023) aggregated time series, as well as the averaged estimate (Table 2). We selected the closest period available (2007−2019) to the one of this study (2007−2021). Our mass change estimate (-26.9 ± 5.3 Gt/a) falls within the methods' spread, but is notably more negative than the averaged estimate of -14.2 ± 7.3 Gt/a. In particular, it is close to the gravimetry estimate (-23.4 ± 5.2 Gt/a). Our mass change estimate for the peripheral glaciers (-13.8 ± 1.4 Gt/a) is four times more negative than the one used in Otosaka et al. (2023) to correct the gravimetry estimate (less than 3 Gt/a). This underlines that correcting for peripheral glacier mass changes is not an easy and straightforward task, and should not be neglected. This also implies that agreement with gravimetry may be coincidental. The mass budget method gives a much more negative mass change (-41.7 ± 5.7 Gt/a) whereas the altimetry provides closer to zero figures (-5.2 ± 2.3 Gt/a). The difference between the altimetry estimate and the estimate from this study, both belonging to the same elevation-differencing group of methods, can come from different sources. If altimetry studies tend to provide generally less negative mass change estimates (e.g. Schröder et al., 2019, Hassan et al., 2025), this is not the case for Smith et al. (2020), who obtained a mass change of -39 ± 5 Gt/a over the period 2003−2019. This more negative value however is linked to very different spatial patterns (see also section 5.1). Some of them are rather unrealistic such as a small portion of the northern tip of the APIS presenting in itself a mass change of -17.7 Gt/a.

Next, we compared the elevation changes obtained over the peripheral glaciers to the three studies mentioned in Fig. 9. The two global studies (Jakob and Gourmelen, 2023 and Hugonnet et al., 2021) do not apply any FAC correction, using instead a constant density conversion factor to get mass changes. Therefore, we directly compared the elevation changes. We obtained more negative elevation change rates compared to the two altimetry studies, which is consistent with the tendency of altimetry to produce less negative estimates over the APIS. Despite the high level of noise coming from the ASTER sensor, the maps from Hugonnet et al. (2021) integrated over the peripheral glaciers produce very similar results to our study. This suggests that observations by DEM differencing are reliably repeatable despite the use of different sensors.

Region	**Study**	**Method**	**Period**	
				dM/dT ($\mathbf{Gt\,a^{-1}}$)
APIS	This study	DEM differencing	2007−2021	-26.5 ± 2.6
	Otosaka et al. (2023)	Altimetry	2007−2019	-5.2 ± 2.3
	Otosaka et al. (2023)	Gravimetry	2007−2019	-23.4 ± 5.2
	Otosaka et al. (2023)	Mass budget method	2007−2019	-41.7 ± 5.7
	Otosaka et al. (2023)	Averaged	2007−2019	-14.2 ± 7.3
	Smith et al. (2020)	Laser altimetry	2003−2019	-39 ± 5
	Hassan et al. (2025)	Laser altimetry	2009−2023	+6.0 ± 2.5
				dh/dT ($\mathbf{m\,a^{-1}}$)
Peripheral glaciers	This study	DEM differencing	2007−2021	-0.16 ± 0.03
	Hassan et al. (2025)	Laser altimetry	2003−2019	-0.05 ± 0.003
	Jakob and Gourmelen (2023)	Radar altimetry	2010−2020	-0.03 ± 0.04
	Hugonnet et al. (2021)	DEM differencing	2007−2020	-0.15 ±0.07

Table 2. Comparison of mass changes over the APIS and elevation changes over the peripheral glaciers. For each study, the method and period selected are indicated. We compare mass change rates over the APIS and elevation change rates over the peripheral glaciers.

https://doi.org/10.5194/egusphere-2026-729
Preprint. Discussion started: 3 March 2026

5.3 Focus on prominent areas

Larsen B embayment

The Larsen B embayment is located on the northeast coast of the AP. It hosted the Larsen B Ice Shelf that was fed by several tributary glaciers until the ice shelf broke up in 2002. This event triggered an intense thinning and acceleration of all tributary glaciers (e.g. Hektoria, Green, Evans, Crane) and has been widely analyzed (e.g. Scambos et al., 2004; Rott et al., 2018). Only a portion of the ice shelf remains, known as the Larsen B remnant or SCAR Inlet Ice Shelf, providing a temporary buttress to Leppard and Flask Glaciers in particular. Other studies have worked on understanding the complex dynamics of the Larsen B Embayment glaciers, showing phases of retreat and re-advance (e.g. Ochwat et al., 2025, Surawy-Stepney et al., 2024, Fluegel and Walker, 2024). The Larsen B Eembayment has been repeatedly identified as the most intensely thinning area of the APIS over the past two decades (e.g. Seehaus et al., 2023, Scambos et al., 2014), and we confirm this. On Hektoria Glacier, the lowest dh_{ice}/dt rates are found between 6 and 16 km upstream from the 2011 glacier's front (before the 2011−2022 readvancement, Fluegel and Walker, 2024), reaching -17.1 m$_{ice}$/a. The same pattern is observed on Green, Evans and Crane Glaciers, where elevation change rates peak a few kilometers away from the glacier front at -13.8 m$_{ice}$/a, -6.7 m$_{ice}$/a and -5.2 m$_{ice}$/a respectively. Leppard and Flask are still buttressed by the SCAR Inlet Ice Shelf, and show less negative dh_{ice}/dt signals (-3.2 m$_{ice}$/a and -2.7 m$_{ice}$/a at minimum). However, the gradual decline in stress caused by the increasing instability of the ice shelf over the period could explain the observed thinning pattern of these two glaciers (Li et al., 2021). Even though the Larsen B tributary glaciers represent only 2% of the AP area, they contribute significantly to the total AP mass losses. Over 2007−2021, Hektoria Glacier (-2.3 ± 0.2 Gt/a) and Green Glacier (-1.80 ± 0.1 Gt/a) are listed among the 30 highest contributors. More generally, the Larsen B tributary glaciers present a total mass change rate of -6.92 ± 0.7 Gt/a, corresponding to 17% of AP mass loss. While those mass changes are in continuity with the 2002−2011 estimate of -8.9 Gt/a from Berthier et al. (2012), the region has by then undergone several major changes as a result of short-term climate trends (e.g. Ochwat et al., 2024) that cannot be disentangled in our analysis.

Fleming Glacier

Fleming is a large glacier located on the southwest coast of the AP, historically feeding an ice shelf in Wordie Bay along with other smaller tributary glaciers (Rotz, Airy, Seller and Prospect). The dynamic evolution of Fleming and its neighbor glaciers after the slow disintegration of the ice shelf between 1960 and the late 1990s has been documented by several studies, in terms of velocity, elevation or grounding line changes. Zhao et al. (2017) reported a decrease of dh/dt comparing the periods 1966−2008 and 2008−2015 over Fleming Glacier. They found elevation change rates of -1.5 m/a at the front of the glacier between 1966 and 2008 and minimum elevation change rates of -1.9 m/a, reached in areas more upstream. Looking at the period 2007−2021, we also obtained elevation change rates much lower than the Zhao et al.'s first period (1966−2008), -2.7 m/a at the glacier front and -6.5 m/a at minimum, corroborating the intensified thinning of Fleming glacier over the past decades. The lowest elevation change rates are located a few kilometers upstream from the glaciers' front, closer to the front than reported by Friedl et al. (2018) over 2011−2014. Our study also shows that Airy glacier presented less negative elevation change rates in comparison to the other glaciers, likely related to a more favorable bedrock geometry. The Fleming catchment, encompassing Fleming, Rotz, Airy, Seller and Prospect glaciers in SIL20 outlines, presented a mass change rate of -5.3 ± 0.2 Gt/a, second largest contribution in ice mass loss over the period 2007−2021. These significant figures suggest that the tributary glaciers of the former Wordie Bay ice shelf are still responding dynamically to its breakup, and that they have not yet found a new equilibrium state by 2021.

Tidewater glaciers of the northwest AP

Tidewater glaciers of the northwest AP have presented different dynamic behaviors over the past few decades, which have been predominantly linked to an oceanic forcing. Cook et al. (2016) identified two different oceanic circulations controlling the position of glacier's front over multidecadal time scales. In the northern part of the AP's west coast, glaciers are exposed to the cool Bransfield Strait Water (BSW). Further south, from Anvers Island until the north of Alexander Island, the oceanic circulation is dominated by the warm Circumpolar Deep Water (CDW). The CDW presents a particular depth pattern: a cooling trend is observed up to 100 m depth, followed by a warming trend below 200 m depth and beyond. According to Cook et al. (2016), this warming is a primary control of the retreat observed for many glacier's front exposed to the CDW.

Investigating the consequences of the subsurface ocean warming, Wallis et al. (2023) documented the evolution of Cadman Glacier over the past three decades. Following a period of front stability until the early 2000s, the glacier started to retreat at a moderate rate. It underwent an intense acceleration event in 2018-2019, which was related to the long-term thinning of its ice shelf. In March 2021, the latter collapsed entirely, leading to a 5.2 km-front retreat and contributing to the glacier's acceleration and thinning. Wallis et al. (2023) report extreme elevation change rates of -20.1 ± 2.6 m/a after the 2019 acceleration, which is indeed lower than our rate of -10 m/a over the period 2007−2021. They highlighted that the dynamic thinning affected inland areas up to 8 km away from the 2015 grounding line. We also identify this propagation of negative elevation rates, but the reported value of -3.0 ± 0.5 m/a is reached 6 km closer to the grounding line. Their work suggests that thinning intensified towards the end of our study period, which would explain why we observed less negative elevation changes over the entire 2007−2021 period.

Unlike Cadman Glacier, the Funk and Lever neighboring glaciers have shown constant velocities and stable terminus over the past decades (Wallis et al., 2023). We confirm that between 2007 and 2021, a much more negative elevation change was obtained for Cadman Glacier (-0.89 ±0.12 m_{ice}/a) than for Funk and Lever Glaciers (-0.06 ±0.08 m_{ice}/a and -0.13 ±0.10 m_{ice}/a, respectively). Moreover, several nearby glaciers presented thickening glacier tongues, including Trooz and Funk Glaciers, which participate in the slightly positive or close-to-zero mean elevation change obtained for these glaciers. Wallis et al. (2023) postulated that the disparities between the recent dynamic evolution of the Cadman Glacier and the neighboring glaciers are related to the different bathymetry configurations. Cadman Glacier was exposed to warm subsurface currents due to a deep frontal fjord, which could have weakened the ice shelf and triggered the glacier's increased ice discharge. On the contrary, Funk and Lever Glaciers were protected from warm oceanic intrusions thanks to their shallow sills. Davison et al. (2024) generalize this relationship between glacier ice discharge and bathymetry to the entire northwestern AP. Between 2017 and 2022, they reported a widespread acceleration and increase in ice discharge of glaciers from this region. They attributed these dramatic changes to the influence of warmer ocean temperatures from the CDW, primarily controlled by the topography of the sills.

Along the Trinity Peninsula and the Davis and Danco Coasts, exposed to the BSW, we observe that glaciers have remained stable or even thickened over the period 2007−2021 (Fig. 7), in accordance with the results from Cook et al. (2016) and Davison et al. (2024). Further south along the western coast, between Anvers and Adelaide Island, elevation changes are mostly negative, except for a few glaciers close to equilibrium. Adelaide, Renaud and Lavoisier Islands also host some of the most thinning glaciers, which is consistent with the CDW predominance in the southwestern part of the AP. However, we observe no clear relationship between elevation changes and Bedmap3 bathymetry at glacier's front for catchments exposed to either CDW or BSW (not shown). As the widespread ice discharge increase reported by Davison et al. (2024) started in ∼2019, at the very end of our study period (2007−2021), it might require more time to initiate significant negative elevation changes. This increase could also be the result of the thickening of glacier tongues observed before 2019 (Fig. 7). Furthermore, the difficulty to constrain bedrock models in many places hinders accurate bathymetry estimates. Large discrepancies appear between the different models (e.g. Shahateet et al., 2023), complicating the identification of significant correlations. More broadly, the relationship between elevation changes and bathymetry at the glacier's front is likely to be more complex than simply depth-dependent. Taking other parameters into account, such as the bed geometry and inclination, could be beneficial to better understand the spatial variability of elevation changes over the northwestern AP.

5.4 Strengths, limitations and perspectives

Elevation corrections

The choice of a GIA or elastic rebound model has minor implications for the final volume changes. The GIA corrections systematically represent less than 4% of the signal, and falls within the observational uncertainty. On the other hand, the four FDMs used in this study lead to significantly different estimates, both in terms of spatial patterns and numerical values. To get a sense of the FAC correction applied, we calculated the mean density corresponding to the volume changes observed. We obtained a density of $878 \pm 62\,\mathrm{kg/m^3}$ (1-σ spread between the models) for the APIS and $843 \pm 50\,\mathrm{kg/m^3}$ for the peripheral glaciers. This number falls into the uncertainty bar of the density conversion factor commonly used by the glacier and ice cap community, $850 \pm 60\,\mathrm{kg/m^3}$ from Huss (2013). However, at the AP scale, the FAC correction induces the largest uncertainty (Fig.A12). It accounts for up to 20% of the signal on some glaciers, with a large spread between the models over the AP, reaching 0.08 m/a at maximum. These discrepancies among the models can be explained by the different settings of the FDMs, based on distinct compaction models and climatic forcings. Another difficulty comes from the scarcity of in situ measurements, which makes it challenging to constrain the models. The period selected to compute the FAC correction (start, end or entire summer) also affects the results at orders of magnitude similar to the spread between the models. Thus, the conversion from volume to mass, applied through the FAC correction, constitutes one of the major limitations of this method. A better understanding of firn processes and firn modeling is therefore a priority to improve the DEM differencing method for glaciers and ice sheets mass changes studies (The Firn Symposium team et al., 2024).

Interpolation

As a third of AP area is not covered by observation data, interpolated data represent a non-negligible part of the final estimates. Over large regions of the APIS, the interpolation represents the second source of uncertainty (Fig.A12). For example, the mass changes obtained for Region 24 using the ZWA12 outlines (-8.0 ± 3.4 Gt/a, Fig. 6a) includes a large uncertainty that is essentially caused by the partial coverage of dh/dt maps (57%). The local hypsometric interpolation performs well in smooth high altitude areas but struggles more reproducing local patterns of intense thinning at lower elevations (e.g. Drygalski or Fleming Glaciers). We suggest the interpolation could be improved by taking into account more input data to explain the spatial variability of the dh/dt signal (e.g. velocity acceleration). As mentioned in section 5.1, another alternative to fill data gaps could be to combine laser altimetry maps, which may allow to better reproduce the spatial patterns.

Grounding line

The grounding line is a physical delimitation difficult to observe, both with in situ and satellite measurements (Friedl et al., 2020). Its location depends on many poorly constrained factors, including bedrock geometry and ice thickness. AP-scale grounding line datasets are scarce and not available at an annual resolution. Nevertheless, rapid fluctuations, including frequent retreat of the grounding line are induced by glacier dynamics at sub-annual scales. In a many areas, the position of the grounding line has not yet been agreed upon (e.g. Hektoria Glacier). Here, considering a 14-year period complicates the choice of grounding line dataset. The grounding line from the first epoch may encompass areas that subsequently became ungrounded, while the one from the second epoch could miss former grounded ice changes. Cadman Glacier illustrates this dilemma, exhibiting pronounced differences between the grounding line datasets used in this study. However, we emphasize that a limited number of AP's glaciers are prone to those grounding line disparities. With the SIL20 outline, Cadman Glacier (Fig. 7) presented mass changes of -0.27 ± 0.02 Gt/a over a total area of 332 km^2. The Bedmap 3 grounding line (Pritchard et al., 2025), located ∼5 km more inland, identifies the lowest portion of the glacier as the ice shelf. This area, covering 15 km^2, lost 0.03 Gt/a, which represents ∼10% of the SIL20 outlines estimate. At the scale of the AP, the mass changes caused by grounding line differences are negligible. Nevertheless, catchment-scale studies might require a more accurate grounding line, including knowledge of its migration.

Time constraints

As each epoch extends over three years, we cannot exclude potential influence of inter annual variations that affect the mass change results, such as the high surface mass balance in 2022 (Wang et al., 2023). Still, we tried to reduce the seasonal influence by establishing strict constraints on the seasonal time difference between the acquisitions. Our elevation change maps are based on the comparison of DEMs over two epochs and hence does not allow us to observe and analyze elevation changes throughout the period. For example, potential variations of the elevation difference rates trends or specific events happening during the time period cannot be isolated in this study. This is quite clear when comparing the results from Scambos et al. (2014) and Seehaus et al. (2023), that cover two distinct time periods and show contrasted elevation changes over the fast-changing glaciers. The extreme changes that Hektoria Glacier underwent over the two past decades (slow retreat between 2002 and 2011, followed by a readvancement until the 1.5-year extreme retreat starting in 2022, Fluegel and Walker, 2024 and Ochwat et al., 2025) cannot be identified either. This is also the case for many other physical processes presenting a strong inter annual variability (e.g. summer melt, Barrand et al., 2013). However, a key advantage of our large study period is that it greatly reduces the noise, especially at high elevations.

6 Conclusions

By combining DEMs derived from stereoscopic images with accurate laser altimetry data, we mapped elevation changes over the Antarctic Peninsula from 2007 to 2021 with substantially improved accuracy and spatial resolution relative to previous studies. Our dataset provides an unprecedented overview of AP glacier mass changes, at regional and local scales, encompassing both the ice sheet and the peripheral glaciers. Taking into account changes in firn air content and crustal rebound processes, we obtained a total mass change of -41.9 ±8.5 Gt/a over the Antarctic Peninsula, equivalent to a sea-level contribution of 0.12 ± 0.02 mm/a (3% of the 2007−2021 sea-level rise). The rate of elevation change for peripheral glaciers (-0.16 ±0.03 m_{ice}/a; i.e. one third of the total mass loss) is slightly more negative than over the ice sheet (-0.11 ±0.01 m_{ice}/a; i.e. two thirds of the total mass loss). We report contrasting regional mass changes, ranging from moderate mass gain in the southeast of the AP to considerable mass losses in all other regions. Investigating the oceanic forcing in the northwestern portion of the AP and the bathymetric correlation of mass losses, we do not find a clear relationship, despite a strong latitudinal pattern of mass changes. However, the elevation change rate maps reveal changes in glaciers that have not received much attention yet, even though they also show striking thinning patterns, such as on Liard Island or the smaller glaciers in Wordie Bay. By reaffirming the importance of regional-scale studies, we also point out the underlying need for an exhaustive list of glacier names and outlines that can be used in consensus by the community. Ultimately, this study also underscores the important role of projects such as SPIRIT and REMA in collecting consistent region-wide datasets, which are essential for gaining a coherent perspective on glacier changes. The continuity of such observations should be a priority of space agencies.

Code and data availability. **Elevation data:** All the SPOT5-HRS stereoscopic pairs were freely downloaded on the REGARDS catalogue at https://regards.cnes.fr/user/swh. ICESat data product ATL06 come from https://nsidc.org/data/atl06/versions/6. ICESat-2 data were accessed through Slide Rule Earth at https://slideruleearth.io. REMA DEMs from Howat et al. (2022a) come from at https://www.pgc.umn.edu/data/rema/. We used the Aviso product of mean sea-level from https://www.aviso.altimetry.fr/msl/. The elevation and mass changes produced in this study will be deposited in a repository upon acceptance of the manuscript.

Firn air content data: Outputs from the GEMB-FDM come from Schlegel and Gardner (2025). Outputs from the IMAU-FDM were downloaded from Veldhuijsen et al. (2025). Outputs from the GSFC-FDM were accessed at Medley et al. (2022a). Outputs from the MAR-FDM come from http://ftp.climato.be/fettweis/MARv3.14/Antarctic/, personnal communication by Xavier Fettweis.

Glacial isostatic adjustment data: Outputs from the Caron et al. (2018) GIA model were accessed at https://vesl.jpl.nasa.gov/solid-earth/gia. We downloaded the outputs from the Whitehouse et al. (2012) GIA model at https://www.pippawhitehouse.com/. Outputs from the Peltier et al. (2015) GIA model come from https://www.atmosp.physics.utoronto.ca/~peltier/data.php.

Code availability: The version 3.3.0 of the software ASP was accessed at https://doi.org/10.5281/zenodo.8270270 (Alexandrov et al., 2023). The *xdem* python package is accessible at https://zenodo.org/records/11492983. The source code of the *LoadDef* model was downloaded from https://github.com/hrmartens/LoadDef. The code developed as part of this study will be deposited in a repository upon acceptance of the manuscript.

Appendix A: Supplementary figures

Author contributions. M.B. performed the analysis and wrote the paper. E.B. initiated the project and coordinated the research. A.D., JMC.B. and D.Y. supported the image extraction and DEM generation. R.H. and A.D. provided inputs on DEM analysis and uncertainty quantification. N.O. and T.S. contributed to the interpretation of the results. P.T.M. and E.C. provided expertise on firn dynamics. L.-M.G. ran the elastic rebound model. All authors contributed to the editing of the manuscript.

Competing interests. We declare that a least one author is a member of the editorial board of The Cryosphere.

Acknowledgements. We thank Livia Jakob for sharing data from Jakob and Gourmelen (2023). We thank Xavier Fettweis for sharing the outputs from MARv3.14 and helping on FAC computation. We thank Nicole Schlegel for sharing the FAC outputs from GEMB model. We thank Ines Otosaka for sharing the IMBIE time series of each method from Otosaka et al. (2023). We thank Hamish Pritchard for sharing the vector product of reconciled grounding lines from Bedmap3 outlines. We thank Lancelot Leclerq for the python technical help and the expertise on sea-level rise.
Financial support: M.B. acknowledges support from the doctoral school SDU2E, Toulouse. E.B. and L.-M.G. acknowledge support from the French Space Agency (CNES).

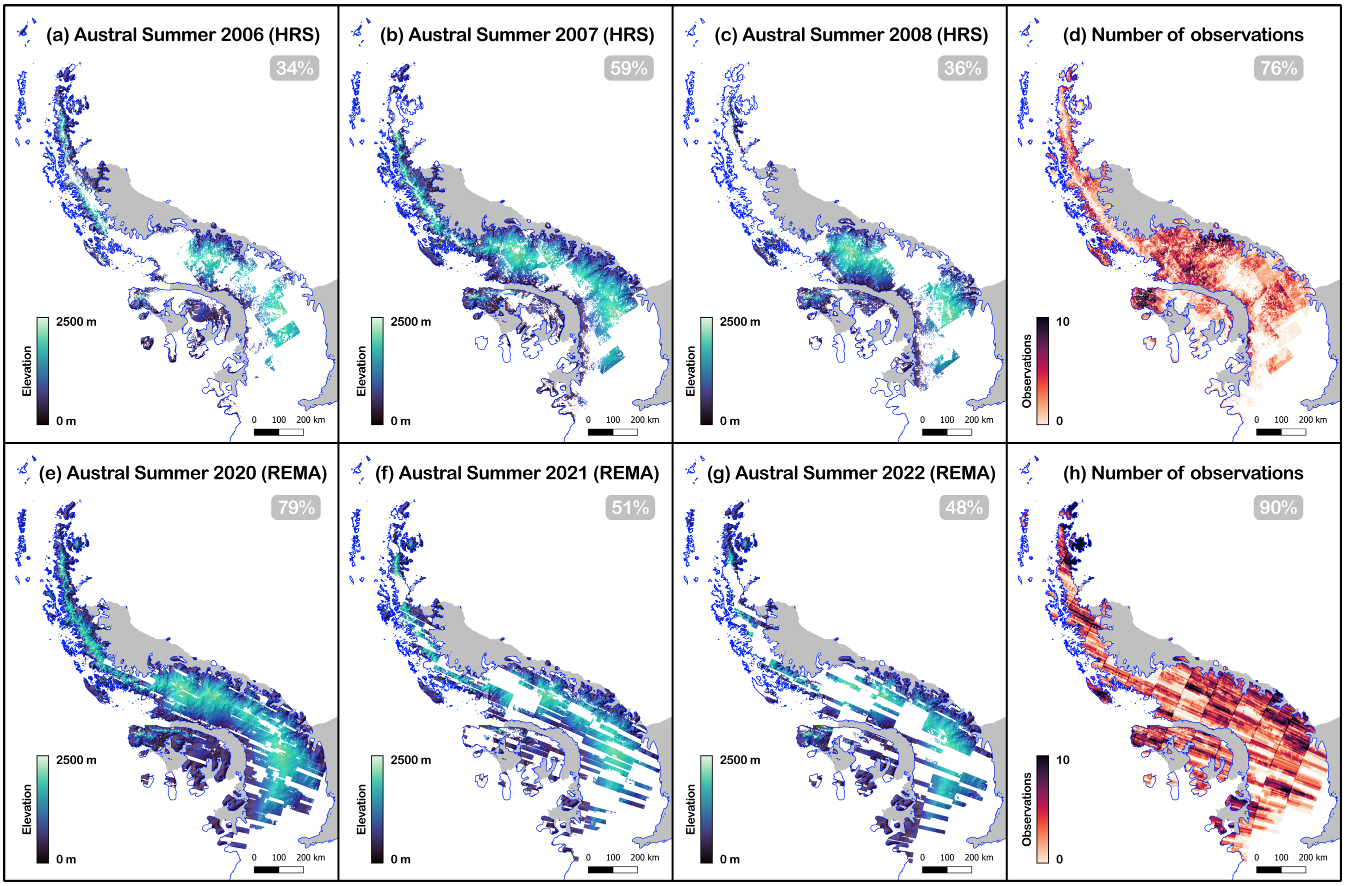

Figure A1. Spatial coverages of SPOT5-HRS segments and REMA DEMs. Spatial coverage of SPOT5-HRS segments for the austral summer 2006 (a), 2007 (b) and 2008 (c). Spatial coverage of REMA DEMs for the austral summer 2020 (e), 2021 (f) and 2022 (g). The total number of observations for each pixel is shown on panels (d) and (h). The percentage of the AP covered area is indicated in the upper right corner of each panel. The Bedmap3 outline of grounded ice is plotted in blue and the ice-shelves are indicated in grey.

References

Alexandrov, O., ScottMcMichael, Broxton, M., Lundy, M., Beyer, R., Husmann, K., Edwards, L., Nefian, A., SmithB, Shean, D., Smith, T., mstyer, Annex, D. A., Moratto, Z., harguess, Dehecq, A., Nodjoumi, G., Aravkin, A., Meyer, J., PicoJr, Bhushan, S., and Laura, J.: NeoGeographyToolkit/StereoPipeline: ASP 3.3.0, https://doi.org/10.5281/zenodo.8270270, 2023.

Bannwart, J., Piermattei, L., Dussaillant, I., Krieger, L., Floricioiu, D., Berthier, E., Roeoesli, C., Machguth, H., and Zemp, M.: Elevation bias due to penetration of spaceborne radar signal on Grosser Aletschgletscher, Switzerland, Journal of Glaciology, 70, e1, https://doi.org/10.1017/jog.2024.37, 2024.

Barrand, N. E., Vaughan, D. G., Steiner, N., Tedesco, M., Kuipers Munneke, P., Van Den Broeke, M. R., and Hosking, J. S.: Trends in Antarctic Peninsula surface melting conditions from observations and regional climate modeling, Journal of Geophysical Research: Earth Surface, 118, 315–330, 2013.

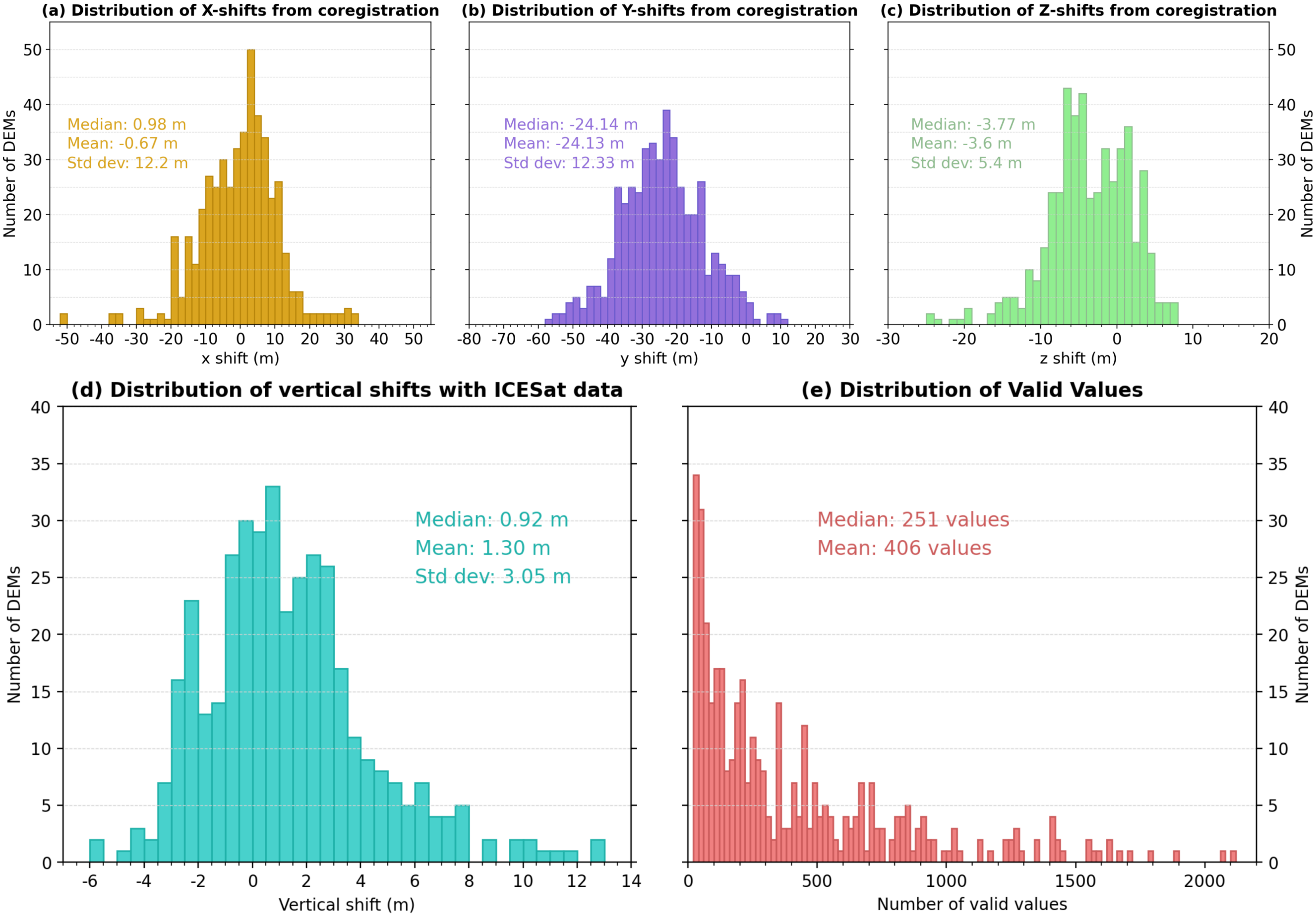

Figure A2. Statistical distributions of coregistration coefficients and vertical adjustment coefficients for HRS DEMs. (a) x-shifts, (b) y-shifts, (c) z-shifts, (d) vertical shift correction applied and (e) number of valid values used (at least 20 for the correction to be applied).

Berthier, E., Scambos, T. A., and Shuman, C. A.: Mass loss of Larsen B tributary glaciers (Antarctic Peninsula) unabated since 2002, Geophysical Research Letters, 39, 2012GL051 755, https://doi.org/10.1029/2012GL051755, 2012.

Berthier, E., Floriciou, D., Gardner, A. S., Gourmelen, N., Jakob, L., Paul, F., Treichler, D., Wouters, B., Belart, J. M. C., Dehecq, A., Dussaillant, I., Hugonnet, R., Kääb, A., Krieger, L., Pálsson, F., and Zemp, M.: Measuring glacier mass changes from space—a review, Reports on Progress in Physics, 86, 036 801, https://doi.org/10.1088/1361-6633/acaf8e, 2023.

Beyer, R. A., Alexandrov, O., and McMichael, S.: The Ames Stereo Pipeline: NASA's Open Source Software for Deriving and Processing Terrain Data, Earth and Space Science, 5, 537–548, https://doi.org/10.1029/2018EA000409, _eprint: https://agupubs.onlinelibrary.wiley.com/doi/pdf/10.1029/2018EA000409, 2018.

Bouillon, A., Bernard, M., Gigord, P., Orsoni, A., Rudowski, V., and Baudoin, A.: SPOT 5 HRS geometric performances: Using block adjustment as a key issue to improve quality of DEM generation, ISPRS Journal of Photogrammetry and Remote Sensing, 60, 134–146, https://doi.org/10.1016/j.isprsjprs.2006.03.002, 2006.

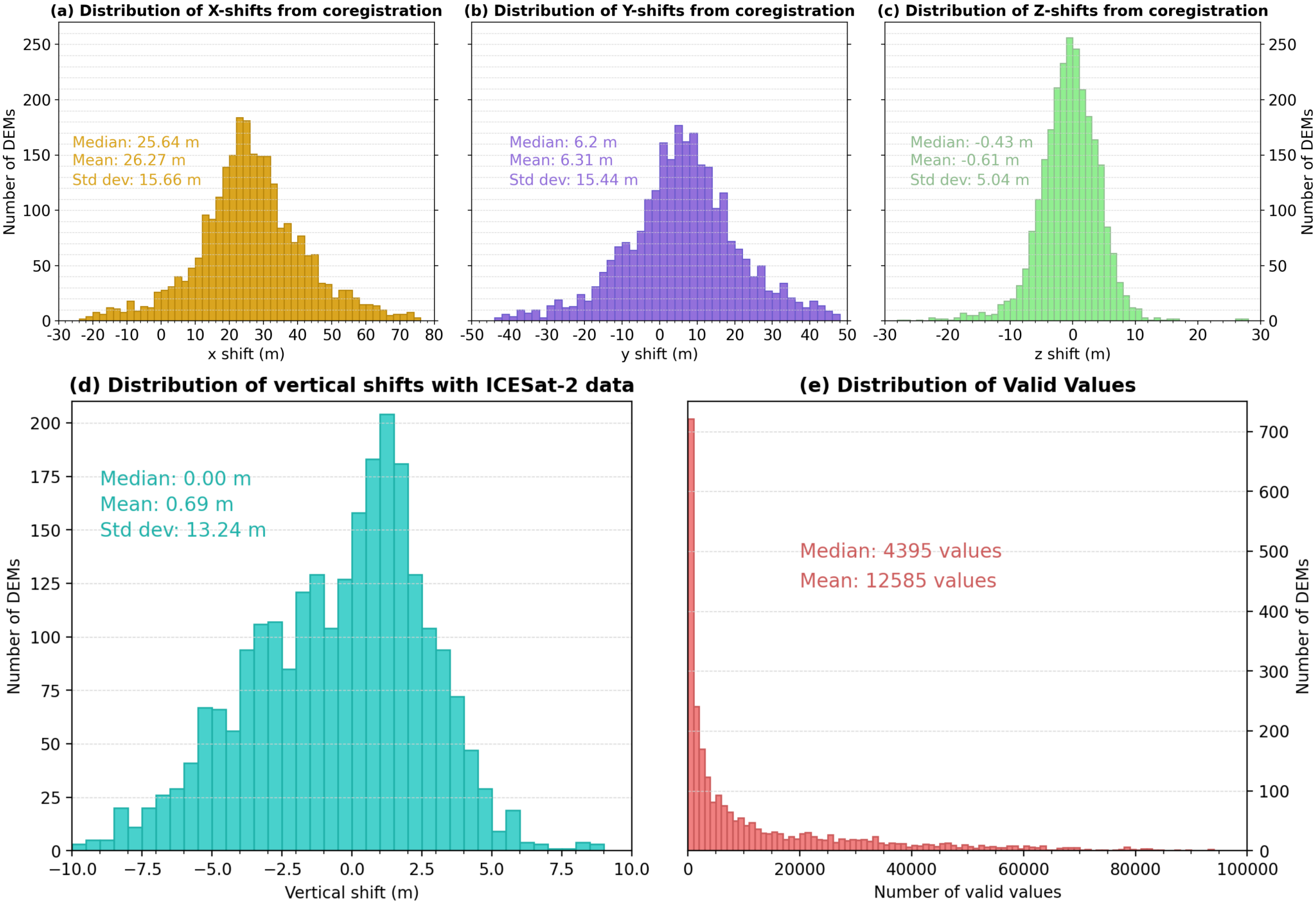

Figure A3. Statistical distributions of coregistration coefficients and vertical adjustment coefficients for REMA DEMs. (a) x-shifts, (b) y-shifts, (c) z-shifts, (d) vertical shift correction applied and (e) number of valid values used (at least 20 for the correction to be applied).

Caron, L., Ivins, E., Larour, E., Adhikari, S., Nilsson, J., and Blewitt, G.: GIA model statistics for GRACE hydrology, cryosphere, and ocean science, Geophysical Research Letters, 45, 2203–2212, 2018.

Cook, A. J., Holland, P. R., Meredith, M. P., Murray, T., Luckman, A., and Vaughan, D. G.: Ocean forcing of glacier retreat in the western Antarctic Peninsula, Science, 353, 283–286, https://doi.org/10.1126/science.aae0017, 2016.

Davison, B. J., Hogg, A. E., Gourmelen, N., Jakob, L., Wuite, J., Nagler, T., Greene, C. A., Andreasen, J., and Engdahl, M. E.: Annual mass budget of Antarctic ice shelves from 1997 to 2021, Science Advances, 9, eadi0186, https://doi.org/10.1126/sciadv.adi0186, 2023.

Davison, B. J., Hogg, A. E., Moffat, C., Meredith, M. P., and Wallis, B. J.: Widespread increase in discharge from west Antarctic Peninsula glaciers since 2018, The Cryosphere, 18, 3237–3251, https://doi.org/10.5194/tc-18-3237-2024, 2024.

Deschamps-Berger, C., Gascoin, S., Berthier, E., Deems, J., Gutmann, E., Dehecq, A., Shean, D., and Dumont, M.: Snow depth mapping from stereo satellite imagery in mountainous terrain: evaluation using airborne laser-scanning data, The Cryosphere, 14, 2925–2940, https://doi.org/10.5194/tc-14-2925-2020, publisher: Copernicus GmbH, 2020.

https://doi.org/10.5194/egusphere-2026-729
Preprint. Discussion started: 3 March 2026

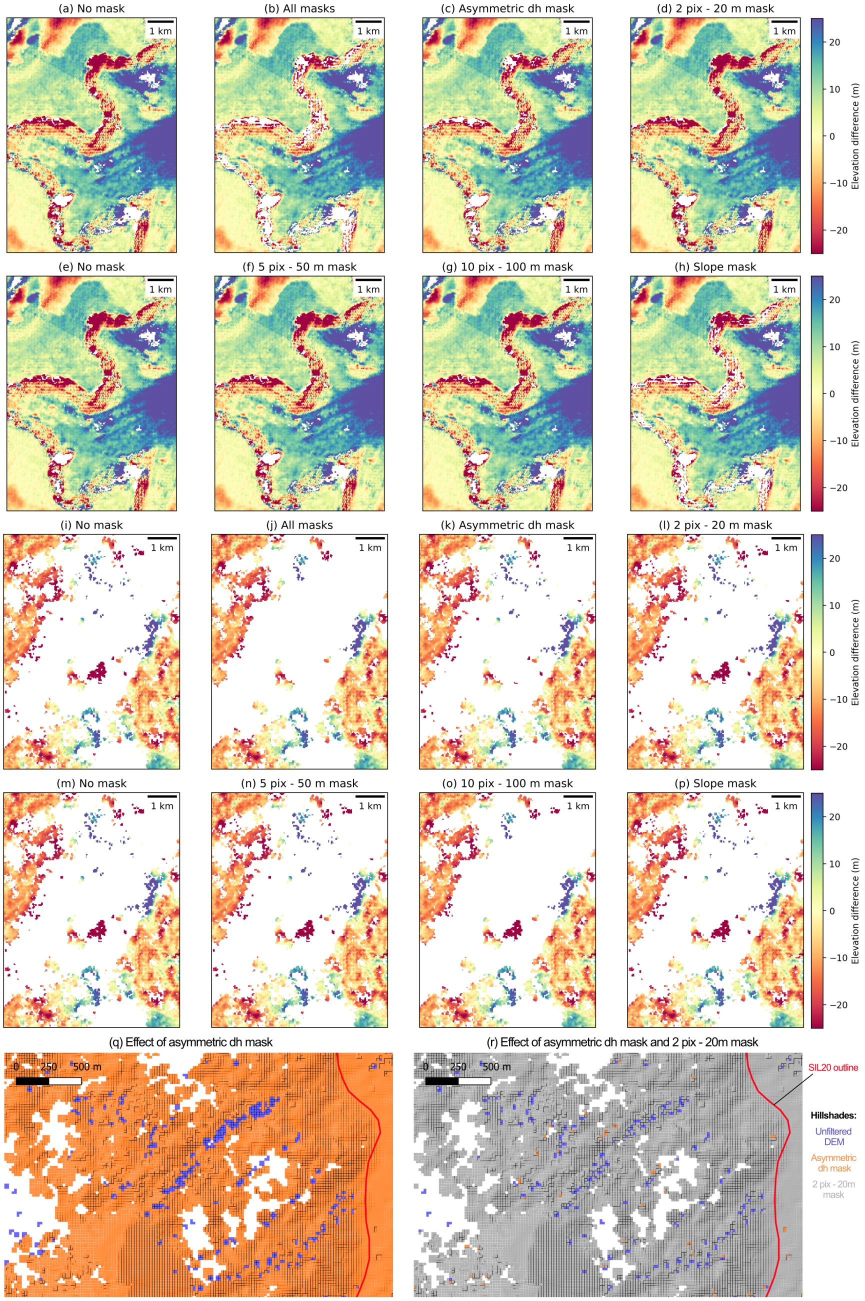

Figure A4. Three case studies of the different DEMs filters. The first zone, plotted on panels (a) to (h), justifies the use of the asymmetric dh mask (c) and the slope mask (h). The second zone illustrate the utility of the asymmetric dh mask (k) and the radius filters (o). The two bottom panels (q) and (r)v show the fruitful combination of the asymmetric filter (orange hillshade) and the radius filter 2 pix - 20 m (grey hillshade) to remove pixel-scale aberrant values from the inital DEM (purple hillshade). The asymmetric filter removes a large part of the outliers (q) but the remaining ones are efficiently removed with the radius filter 2 pix - 20 m (r).

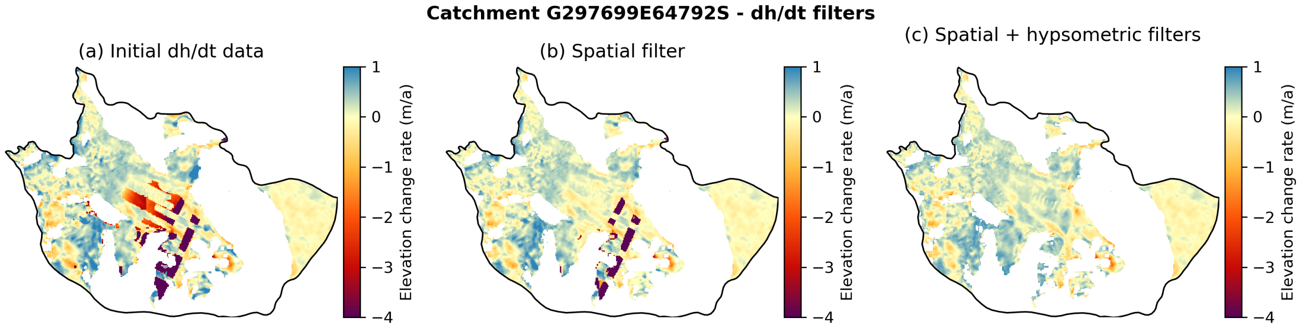

Figure A5. Effects of dh/dt filters on an example catchment. (a) Initial dh/dt data, (b) dh/dt data after spatial filtering, (c) dh/dt data after spatial and hypsometric filters.

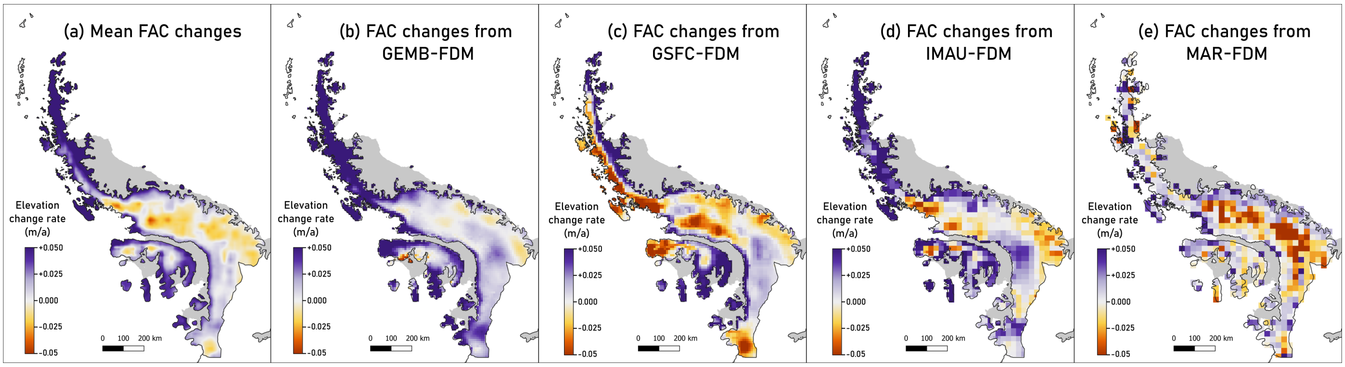

Figure A6. FAC elevation change rates from firn densification models (2007−2021). The mean FAC elevation change rate is shown on the panel (a) and the FAC elevation change rates coming from the different FDMs are plotted on the panels (b)−(e).

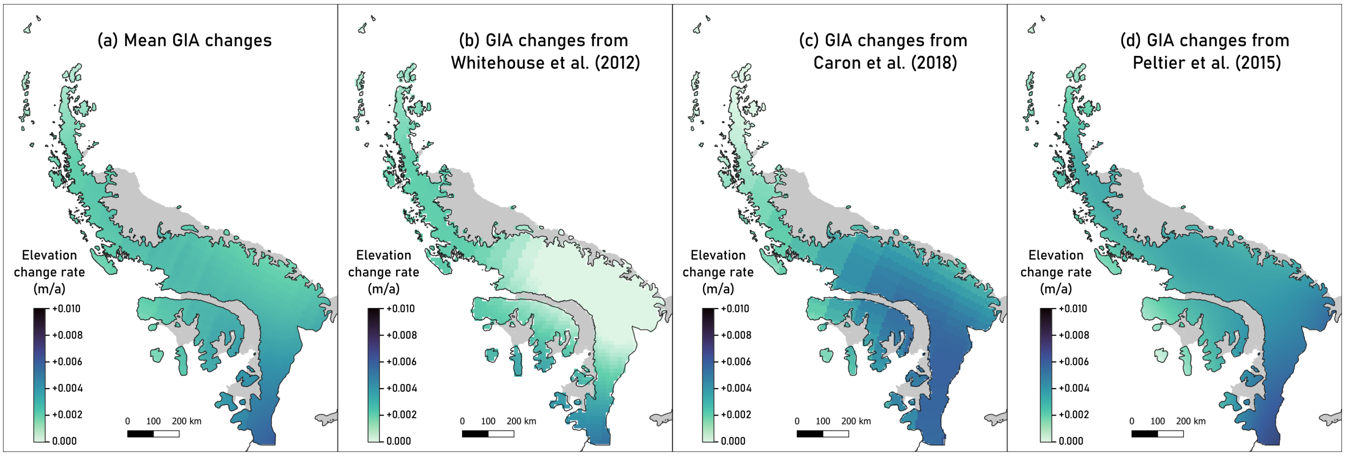

Figure A7. Elevation change rates from GIA models (2007−2021). The mean GIA elevation change rate is shown on the panel (a) and the elevation change rates coming from the different models are plotted on the panels (b)−(d).

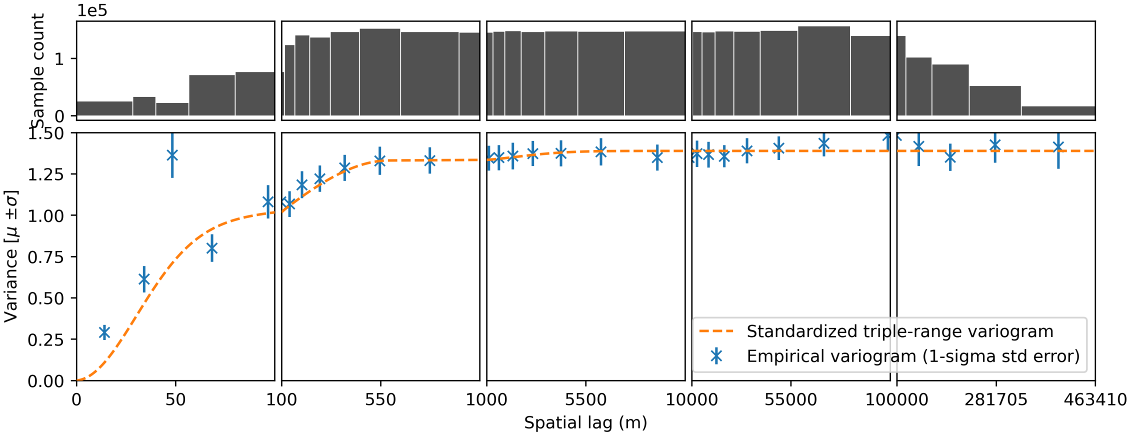

Figure A8. HRS variogram computed from the 13 HRS coincident pairs. The empirical variogram and the associated 1-σ standard deviation error is plotted in blue crosses. The modeled variogram based on the sum of three functions (two gaussians and a spherical) is shown in orange. The range and sill of the three ranges modeled are the following: range_1=86 m, sill_1 = 0.92 (spherical), range_2=596 m, sill_2 = 0.41 (gaussian) and range_3=6 523 m, sill_3 = 0.06 (gaussian).

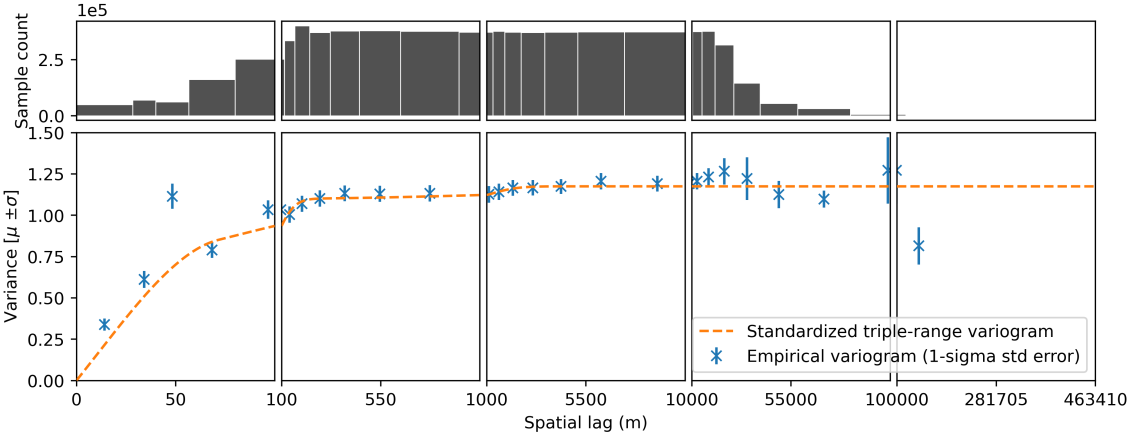

Figure A9. REMA variogram computed from the 23 REMA coincident pairs. The empirical variogram and the associated 1-σ standard deviation error is plotted in blue crosses. The modeled variogram based on the sum of three functions (two gaussians and a spherical) is shown in orange. The range and sill of the three ranges modeled are the following: range_1=71 m, sill_1 = 0.71 (spherical), range_2=217 m, sill_2 = 0.38 (gaussian) and range_3=3 342 m, sill_3 = 0.07 (gaussian).

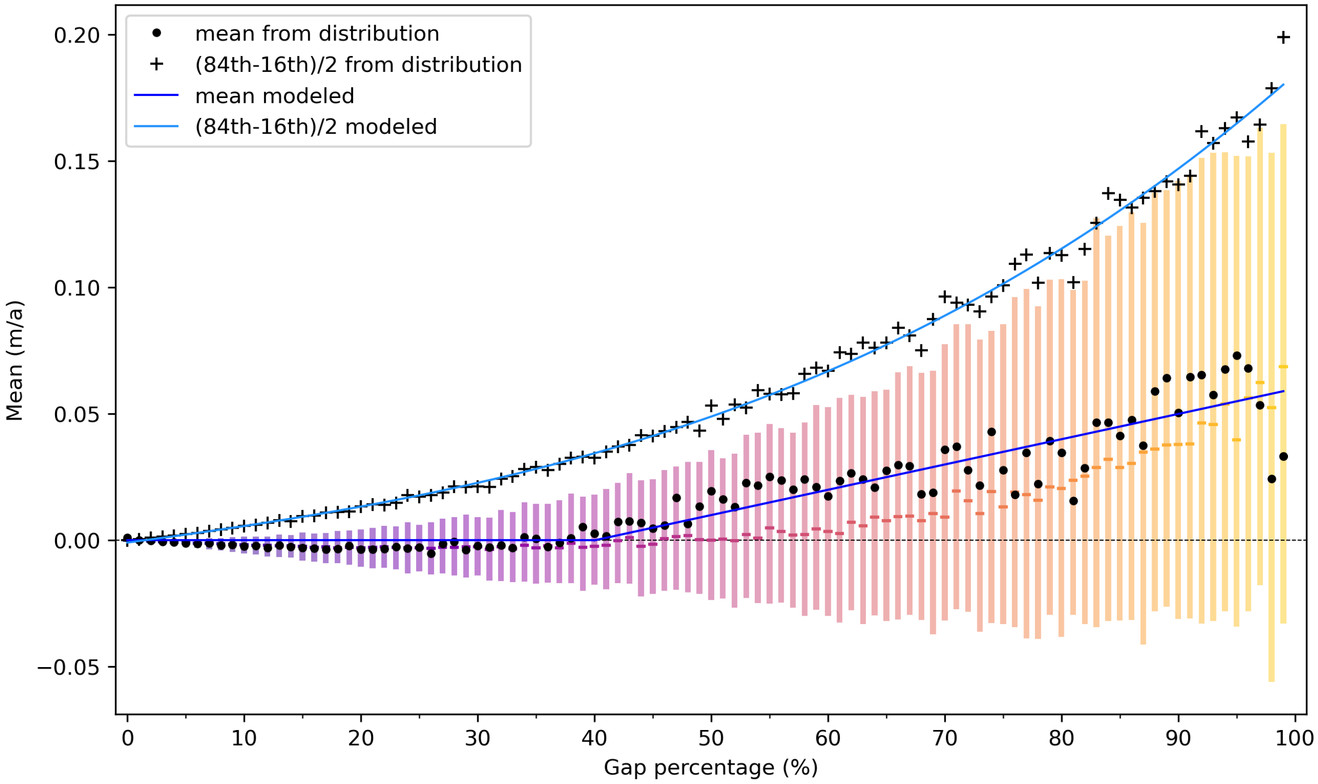

Figure A10. Relationship between the gap size in percentage of the total area and metrics of the mean difference between original and artificially voided dh/dt maps. For each gap size percent, the boxplot (median, 1^{st} and 3^{rd} quartiles) of the means is plotted in color. The mean is shown as a black dot and the robust dispersion metric (84^{th} percentile - 16^{th} percentile)/2 as a black cross. The piecewise-defined function fitted to the series of mean is shown in dark blue and the 3-degree polynomial function fitted to the robust dispersion metric series in light blue.

Dong, Y., Zhao, J., Floricioiu, D., Krieger, L., Fritz, T., and Eineder, M.: High-resolution topography of the Antarctic Peninsula combining the TanDEM-X DEM and Reference Elevation Model of Antarctica (REMA) mosaic, The Cryosphere, 15, 4421–4443, https://doi.org/10.5194/tc-15-4421-2021, 2021.

Dowd, P. A.: The Variogram and Kriging: Robust and Resistant Estimators, pp. 91–106, Springer Netherlands, Dordrecht, ISBN 978-94-009-3699-7, https://doi.org/10.1007/978-94-009-3699-7_6, 1984.

Dziewonski, A. M. and Anderson, D. L.: Preliminary reference Earth model, Physics of the earth and planetary interiors, 25, 297–356, 1981.

Fettweis, X. and Grailet, J.-F.: MAR (Modèle Atmosphérique Régional) version 3.14, https://doi.org/10.5281/zenodo.13151275, 2024.

Fluegel, B. L. and Walker, C.: The Two-Decade Evolution of Antarctica's Hektoria Glacier and Its 2022 Rapid Retreat From Satellite Observations, Geophysical Research Letters, 51, e2024GL110 592, https://doi.org/10.1029/2024GL110592, _eprint: https://agupubs.onlinelibrary.wiley.com/doi/pdf/10.1029/2024GL110592, 2024.

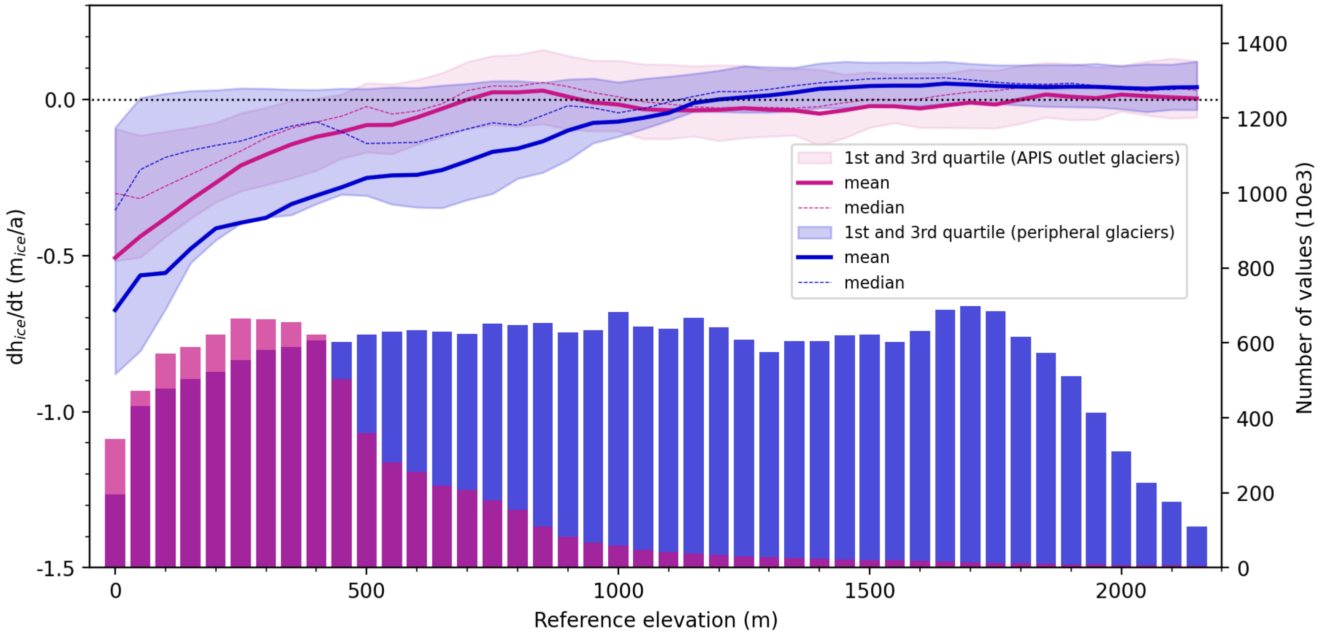

Figure A11. Hypsometric signal of ice elevation changes over the APIS (blue) and the peripheral glaciers (purple). For the two categories, the histograms at the bottom show the distribution of elevations. The distribution (median, mean, 1st and 3rd quartiles) of dh/dt values per elevation bin are plotted at the top.

Friedl, P., Seehaus, T. C., Wendt, A., Braun, M. H., and Höppner, K.: Recent dynamic changes on Fleming Glacier after the disintegration of Wordie Ice Shelf, Antarctic Peninsula, The Cryosphere, 12, 1347–1365, https://doi.org/10.5194/tc-12-1347-2018, publisher: Copernicus GmbH, 2018.

780 Friedl, P., Weiser, F., Fluhrer, A., and Braun, M. H.: Remote sensing of glacier and ice sheet grounding lines: A review, Earth-Science Reviews, 201, 102 948, https://doi.org/10.1016/j.earscirev.2019.102948, 2020.

Gardner, A. S., Schlegel, N.-J., and Larour, E.: Glacier Energy and Mass Balance (GEMB): a model of firn processes for cryosphere research, Geoscientific Model Development, 16, 2277–2302, https://doi.org/10.5194/gmd-16-2277-2023, 2023.

Gelaro, R., McCarty, W., Suárez, M. J., Todling, R., Molod, A., Takacs, L., Randles, C. A., Darmenov, A., Bosilovich, M. G., Reichle, R., et al.: The modern-era retrospective analysis for research and applications, version 2 (MERRA-2), Journal of climate, 30, 5419–5454, 2017. 785

German Aerospace Center: TanDEM-X - Digital Elevation Model (DEM) - Global, 90m, https://doi.org/10.15489/JU28HC7PUI09, 2018.

Hassan, J., van den Broeke, M. R., Veldhuijsen, S. B., Colgan, W., Berg, D. L., Lippert, E. Y. H., and Khan, S. A.: Mass loss of Greenland and Antarctic peripheral glaciers from ICESat and ICESat-2, Journal of Geophysical Research: Earth Surface, 130, e2024JF007 989, 2025.

790 Hirschmuller, H.: Stereo Processing by Semiglobal Matching and Mutual Information, IEEE Transactions on Pattern Analysis and Machine Intelligence, 30, 328–341, https://doi.org/10.1109/TPAMI.2007.1166, 2008.

Hock, R., Maussion, F., Marzeion, B., and Nowicki, S.: What is the global glacier ice volume outside the ice sheets?, Journal of Glaciology, 69, 204–210, https://doi.org/10.1017/jog.2023.1, 2023.

https://doi.org/10.5194/egusphere-2026-729
Preprint. Discussion started: 3 March 2026

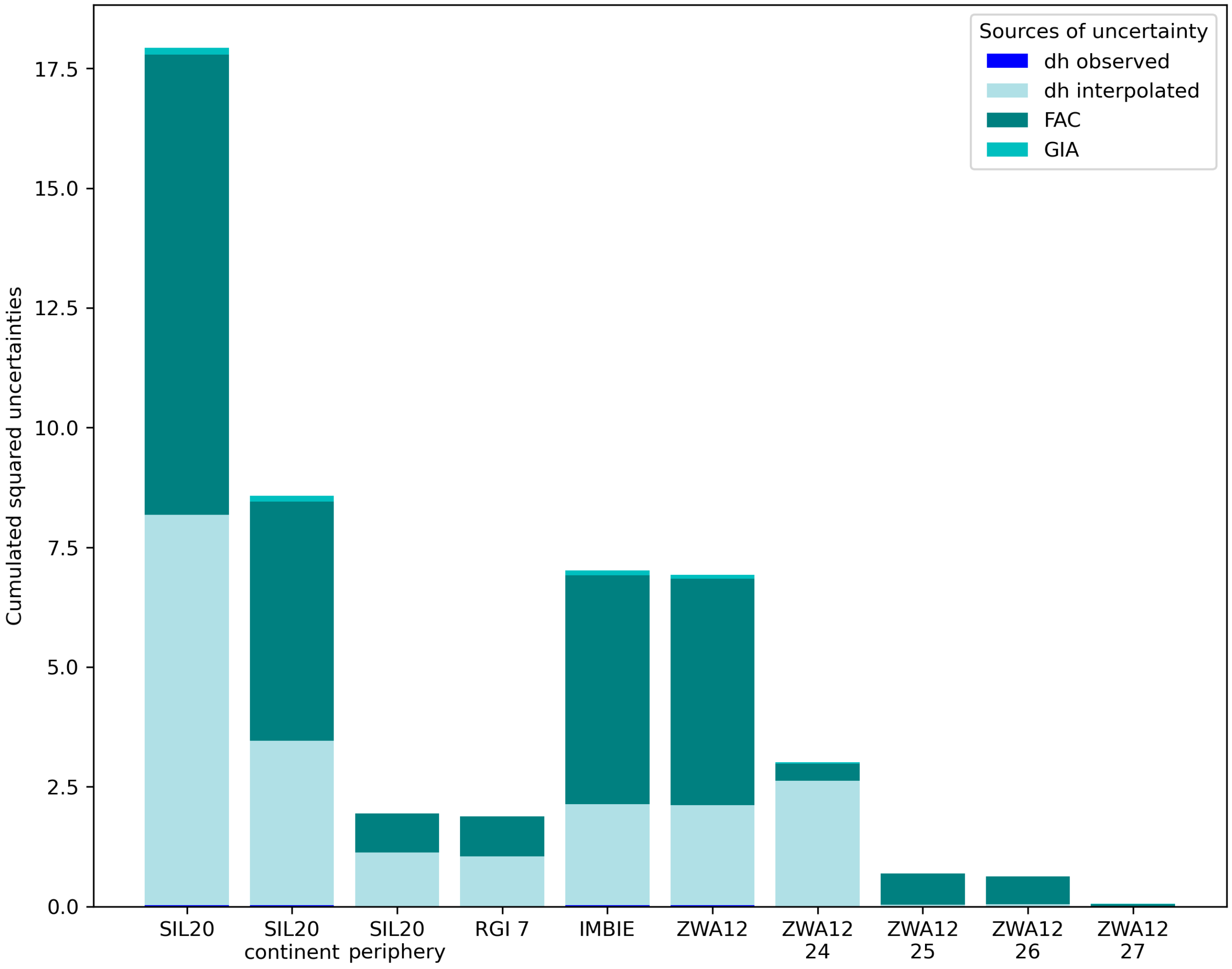

Figure A12. Contributions of sources of uncertainty for the main regions of the AP. For each outline, the different sources of uncertainties are plotted as a cumulative barplot.

https://doi.org/10.5194/egusphere-2026-729
Preprint. Discussion started: 3 March 2026

Howat, I., Porter, C., Noh, M.-J., Husby, E., Khuvis, S., Danish, E., Tomko, K., Gardiner, J., Negrete, A., Yadav, B., Klassen, J., Kelleher, C., Cloutier, M., Bakker, J., Enos, J., Arnold, G., Bauer, G., and Morin, P.: The Reference Elevation Model of Antarctica - Strips, Version 4.1, https://doi.org/10.7910/DVN/X7NDNY, 2022a.

Howat, I., Porter, C., Noh, M.-J., Husby, E., Khuvis, S., Danish, E., Tomko, K., Gardiner, J., Negrete, A., Yadav, B., Klassen, J., Kelleher, C., Cloutier, M., Bakker, J., Enos, J., Arnold, G., Bauer, G., and Morin, P.: The Reference Elevation Model of Antarctica - Strips, Version 4.1, https://doi.org/10.7910/DVN/X7NDNY, 2022b.

Howat, I. M., Porter, C., Smith, B. E., Noh, M.-J., and Morin, P.: The Reference Elevation Model of Antarctica, The Cryosphere, 13, 665–674, https://doi.org/10.5194/tc-13-665-2019, 2019.

Hugonnet, R., McNabb, R., Berthier, E., Menounos, B., Nuth, C., Girod, L., Farinotti, D., Huss, M., Dussaillant, I., Brun, F., and Kääb, A.: Accelerated global glacier mass loss in the early twenty-first century, Nature, 592, 726–731, https://doi.org/10.1038/s41586-021-03436-z, publisher: Nature Publishing Group, 2021.

Hugonnet, R., Brun, F., Berthier, E., Dehecq, A., Mannerfelt, E. S., Eckert, N., and Farinotti, D.: Uncertainty Analysis of Digital Elevation Models by Spatial Inference From Stable Terrain, IEEE Journal of Selected Topics in Applied Earth Observations and Remote Sensing, 15, 6456–6472, https://doi.org/10.1109/JSTARS.2022.3188922, 2022.

Huss, M.: Density assumptions for converting geodetic glacier volume change to mass change, The Cryosphere, 7, 877–887, https://doi.org/10.5194/tc-7-877-2013, 2013.

Jakob, L. and Gourmelen, N.: Glacier mass loss between 2010 and 2020 dominated by atmospheric forcing, Geophysical Research Letters, 50, e2023GL102 954, 2023.

Korona, J., Berthier, E., Bernard, M., Rémy, F., and Thouvenot, E.: SPIRIT. SPOT 5 stereoscopic survey of Polar Ice: Reference Images and Topographies during the fourth International Polar Year (2007–2009), ISPRS Journal of Photogrammetry and Remote Sensing, 64, 204–212, https://doi.org/10.1016/j.isprsjprs.2008.10.005, 2009.

Kunz, M., King, M. A., Mills, J. P., Miller, P. E., Fox, A. J., Vaughan, D. G., and Marsh, S. H.: Multi-decadal glacier surface lowering in the Antarctic Peninsula, Geophysical Research Letters, 39, 2012.

Le Rest, K., Pinaud, D., Monestiez, P., Chadoeuf, J., and Bretagnolle, V.: Spatial leave-one-out cross-validation for variable selection in the presence of spatial autocorrelation, Global Ecology and Biogeography, 23, 811–820, https://doi.org/10.1111/geb.12161, 2014.

Li, Y., Qiao, G., and Yuan, X.: OBSERVATIONS OF CONTINUOUS INSTABILITY FOR SCAR INLET ICE SHELF, ANTARCTIC PENINSULA, The International Archives of the Photogrammetry, Remote Sensing and Spatial Information Sciences, XLIII-B3-2021, 485–490, https://doi.org/10.5194/isprs-archives-XLIII-B3-2021-485-2021, 2021.

Markus, T., Neumann, T., Martino, A., Abdalati, W., Brunt, K., Csatho, B., Farrell, S., Fricker, H., Gardner, A., Harding, D., Jasinski, M., Kwok, R., Magruder, L., Lubin, D., Luthcke, S., Morison, J., Nelson, R., Neuenschwander, A., Palm, S., Popescu, S., Shum, C., Schutz, B. E., Smith, B., Yang, Y., and Zwally, J.: The Ice, Cloud, and land Elevation Satellite-2 (ICESat-2): Science requirements, concept, and implementation, Remote Sensing of Environment, 190, 260–273, https://doi.org/10.1016/j.rse.2016.12.029, 2017.

Martens, H. R., Rivera, L., and Simons, M.: LoadDef: A Python-Based Toolkit to Model Elastic Deformation Caused by Surface Mass Loading on Spherically Symmetric Bodies, Earth and Space Science, 6, 311–323, https://doi.org/10.1029/2018EA000462, _eprint: https://agupubs.onlinelibrary.wiley.com/doi/pdf/10.1029/2018EA000462, 2019.

McNabb, R., Nuth, C., Kääb, A., and Girod, L.: Sensitivity of glacier volume change estimation to DEM void interpolation, The Cryosphere, 13, 895–910, https://doi.org/10.5194/tc-13-895-2019, 2019.

Medley, B., Neumann, T., Zwally, H. J., Smith, B. E., and Stevens, C. M.: NASA GSFC Firn Densification Model version 1.2.1 (GSFC-FDMv1.2.1) for the Greenland and Antarctic Ice Sheets: 1980-2021, https://doi.org/10.5281/zenodo.7054574, 2022a.

Medley, B., Neumann, T. A., Zwally, H. J., Smith, B. E., and Stevens, C. M.: Simulations of firn processes over the Greenland and Antarctic ice sheets: 1980–2021, The Cryosphere, 16, 3971–4011, https://doi.org/10.5194/tc-16-3971-2022, publisher: Copernicus GmbH, 2022b.

Nilsson, J., Gardner, A. S., and Paolo, F. S.: Elevation change of the Antarctic Ice Sheet: 1985 to 2020, Earth System Science Data, 14, 3573–3598, https://doi.org/10.5194/essd-14-3573-2022, 2022.

Noh, M.-J. and Howat, I. M.: Automated stereo-photogrammetric DEM generation at high latitudes: Surface Extraction with TIN-based Search-space Minimization (SETSM) validation and demonstration over glaciated regions, GIScience & Remote Sensing, 52, 198–217, https://doi.org/10.1080/15481603.2015.1008621, _eprint: https://doi.org/10.1080/15481603.2015.1008621, 2015.

Noh, M.-J. and Howat, I. M.: The Surface Extraction from TIN based Search-space Minimization (SETSM) algorithm, ISPRS Journal of Photogrammetry and Remote Sensing, 129, 55–76, https://doi.org/10.1016/j.isprsjprs.2017.04.019, 2017.

Nuth, C. and Kääb, A.: Co-registration and bias corrections of satellite elevation data sets for quantifying glacier thickness change, The Cryosphere, 5, 271–290, https://doi.org/10.5194/tc-5-271-2011, publisher: Copernicus GmbH, 2011.

Ochwat, N., Scambos, T., Anderson, R. S., Winberry, J. P., Luckman, A., Berthier, E., Bernat, M., and Antropova, Y. K.: Record grounded glacier retreat caused by an ice plain calving process, NATURE GEOSCIENCE, 18, 1117–1124, 2025.

Ochwat, N. E., Scambos, T. A., Banwell, A. F., Anderson, R. S., Maclennan, M. L., Picard, G., Shates, J. A., Marinsek, S., Margonari, L., Truffer, M., and Pettit, E. C.: Triggers of the 2022 Larsen B multi-year landfast sea ice breakout and initial glacier response, The Cryosphere, 18, 1709–1731, https://doi.org/10.5194/tc-18-1709-2024, publisher: Copernicus GmbH, 2024.

Orr, A., Marshall, G. J., Hunt, J. C. R., Sommeria, J., Wang, C.-G., Lipzig, N. P. M. v., Cresswell, D., and King, J. C.: Characteristics of Summer Airflow over the Antarctic Peninsula in Response to Recent Strengthening of Westerly Circumpolar Winds, Journal of the Atmospheric Sciences, 65, 1396–1413, https://doi.org/10.1175/2007JAS2498.1, publisher: American Meteorological Society Section: Journal of the Atmospheric Sciences, 2008.

Otosaka, I. N., Shepherd, A., Ivins, E. R., Schlegel, N.-J., Amory, C., Van Den Broeke, M. R., Horwath, M., Joughin, I., King, M. D., Krinner, G., Nowicki, S., Payne, A. J., Rignot, E., Scambos, T., Simon, K. M., Smith, B. E., Sørensen, L. S., Velicogna, I., Whitehouse, P. L., A, G., Agosta, C., Ahlstrøm, A. P., Blazquez, A., Colgan, W., Engdahl, M. E., Fettweis, X., Forsberg, R., Gallée, H., Gardner, A., Gilbert, L., Gourmelen, N., Groh, A., Gunter, B. C., Harig, C., Helm, V., Khan, S. A., Kittel, C., Konrad, H., Langen, P. L., Lecavalier, B. S., Liang, C.-C., Loomis, B. D., McMillan, M., Melini, D., Mernild, S. H., Mottram, R., Mouginot, J., Nilsson, J., Noël, B., Pattle, M. E., Peltier, W. R., Pie, N., Roca, M., Sasgen, I., Save, H. V., Seo, K.-W., Scheuchl, B., Schrama, E. J. O., Schröder, L., Simonsen, S. B., Slater, T., Spada, G., Sutterley, T. C., Vishwakarma, B. D., Van Wessem, J. M., Wiese, D., Van Der Wal, W., and Wouters, B.: Mass balance of the Greenland and Antarctic ice sheets from 1992 to 2020, Earth System Science Data, 15, 1597–1616, https://doi.org/10.5194/essd-15-1597-2023, 2023.

Peltier, W. R., Argus, D., and Drummond, R.: Space geodesy constrains ice age terminal deglaciation: The global ICE-6G_C (VM5a) model, Journal of Geophysical Research: Solid Earth, 120, 450–487, 2015.

Pfeffer, W. T., Arendt, A. A., Bliss, A., Bolch, T., Cogley, J. G., Gardner, A. S., Hagen, J.-O., Hock, R., Kaser, G., Kienholz, C., and et al.: The Randolph Glacier Inventory: a globally complete inventory of glaciers, Journal of Glaciology, 60, 537–552, https://doi.org/10.3189/2014JoG13J176, 2014.

Pritchard, H. D., Fretwell, P. T., Fremand, A. C., Bodart, J. A., Kirkham, J. D., Aitken, A., Bamber, J., Bell, R., Bianchi, C., Bingham, R. G., Blankenship, D. D., Casassa, G., Christianson, K., Conway, H., Corr, H. F. J., Cui, X., Damaske, D., Damm, V., Dorschel, B., Drews, R., Eagles, G., Eisen, O., Eisermann, H., Ferraccioli, F., Field, E., Forsberg, R., Franke, S., Goel, V., Gogineni, S. P., Greenbaum, J., Hills, B., Hindmarsh, R. C. A., Hoffman, A. O., Holschuh, N., Holt, J. W., Humbert, A., Jacobel, R. W., Jansen, D., Jenkins, A., Jokat, W., Jong, L., Jordan, T. A., King, E. C., Kohler, J., Krabill, W., Maton, J., Gillespie, M. K., Langley, K., Lee, J., Leitchenkov, G., Leuschen, C., Luyendyk, B., MacGregor, J. A., MacKie, E., Moholdt, G., Matsuoka, K., Morlighem, M., Mouginot, J., Nitsche, F. O., Nost, O. A., Paden, J., Pattyn, F., Popov, S., Rignot, E., Rippin, D. M., Rivera, A., Roberts, J. L., Ross, N., Ruppel, A., Schroeder, D. M., Siegert, M. J., Smith, A. M., Steinhage, D., Studinger, M., Sun, B., Tabacco, I., Tinto, K. J., Urbini, S., Vaughan, D. G., Wilson, D. S., Young, D. A., and Zirizzotti, A.: Bedmap3 updated ice bed, surface and thickness gridded datasets for Antarctica, Scientific Data, 12, 414, https://doi.org/10.1038/s41597-025-04672-y, publisher: Nature Publishing Group, 2025.

RGI Consortium: Randolph Glacier Inventory - A Dataset of Global Glacier Outlines, Version 7, https://doi.org/10.5067/F6JMOVY5NAVZ, 2023.

Rignot, E., Jacobs, S., Mouginot, J., and Scheuchl, B.: Ice-Shelf Melting Around Antarctica, Science, 341, 266–270, https://doi.org/10.1126/science.1235798, 2013.

Rignot, E., Mouginot, J., Scheuchl, B., van den Broeke, M., van Wessem, M. J., and Morlighem, M.: Four decades of Antarctic Ice Sheet mass balance from 1979–2017, Proceedings of the National Academy of Sciences, 116, 1095–1103, https://doi.org/10.1073/pnas.1812883116, company: National Academy of Sciences Distributor: National Academy of Sciences Institution: National Academy of Sciences Label: National Academy of Sciences Publisher: Proceedings of the National Academy of Sciences, 2019.

Roberts, D. R., Bahn, V., Ciuti, S., Boyce, M. S., Elith, J., Guillera-Arroita, G., Hauenstein, S., Lahoz-Monfort, J. J., Schröder, B., Thuiller, W., Warton, D. I., Wintle, B. A., Hartig, F., and Dormann, C. F.: Cross-validation strategies for data with temporal, spatial, hierarchical, or phylogenetic structure, Ecography, 40, 913–929, https://doi.org/10.1111/ecog.02881, 2017.

Rolstad, C., Haug, T., and Denby, B.: Spatially integrated geodetic glacier mass balance and its uncertainty based on geostatistical analysis: application to the western Svartisen ice cap, Norway, Journal of Glaciology, 55, 666–680, https://doi.org/10.3189/002214309789470950, 2009.

Rott, H., Abdel Jaber, W., Wuite, J., Scheiblauer, S., Floricioiu, D., Van Wessem, J. M., Nagler, T., Miranda, N., and Van Den Broeke, M. R.: Changing pattern of ice flow and mass balance for glaciers discharging into the Larsen A and B embayments, Antarctic Peninsula, 2011 to 2016, The Cryosphere, 12, 1273–1291, https://doi.org/10.5194/tc-12-1273-2018, 2018.

Rott, H., Scheiblauer, S., Wuite, J., Krieger, L., Floricioiu, D., Rizzoli, P., Libert, L., and Nagler, T.: Penetration of interferometric radar signals in Antarctic snow, The Cryosphere, 15, 4399–4419, https://doi.org/10.5194/tc-15-4399-2021, 2021.

Sanchez Lofficial, A., Métivier, L., Fleitout, L., Chanard, K., Greff-Lefftz, M., de La Serve, M., Gauer, L.-M., and Gourrion, E.: Multi-technique estimation of ice mass balance in Greenland: impact of the uncertainties on firn densification and GIA models, Geophysical Journal International, 240, 1935–1952, https://doi.org/10.1093/gji/ggaf015, publisher: Oxford University Press (OUP), 2025.

Scambos, T. A., Bohlander, J. A., Shuman, C. A., and Skvarca, P.: Glacier acceleration and thinning after ice shelf collapse in the Larsen B embayment, Antarctica, Geophysical Research Letters, 31, 2004GL020 670, https://doi.org/10.1029/2004GL020670, 2004.

Scambos, T. A., Berthier, E., Haran, T., Shuman, C. A., Cook, A. J., Ligtenberg, S. R. M., and Bohlander, J.: Detailed ice loss pattern in the northern Antarctic Peninsula: widespread decline driven by ice front retreats, The Cryosphere, 8, 2135–2145, https://doi.org/10.5194/tc-8-2135-2014, 2014.

Schannwell, C., Barrand, N. E., and Radić, V.: Future sea-level rise from tidewater and ice-shelf tributary glaciers of the Antarctic Peninsula, Earth and Planetary Science Letters, 453, 161–170, 2016.

Schlegel, N.-J. and Gardner, A.: Output from the Glacier Energy and Mass Balance (GEMB v1.0) forced with 3-hourly ERA5 fields and gridded to 10km, Greenland and Antarctica 1979-2024, https://doi.org/10.5281/zenodo.14714746, 2025.

https://doi.org/10.5194/egusphere-2026-729
Preprint. Discussion started: 3 March 2026

Schröder, L., Horwath, M., Dietrich, R., Helm, V., Van Den Broeke, M. R., and Ligtenberg, S. R. M.: Four decades of Antarctic surface elevation changes from multi-mission satellite altimetry, The Cryosphere, 13, 427–449, https://doi.org/10.5194/tc-13-427-2019, 2019.

Schutz, B. E., Zwally, H. J., Shuman, C. A., Hancock, D., and DiMarzio, J. P.: Overview of the ICESat Mission, Geophysical Research Letters, 32, https://doi.org/10.1029/2005GL024009, _eprint: https://agupubs.onlinelibrary.wiley.com/doi/pdf/10.1029/2005GL024009, 2005.

Seehaus, T., Sommer, C., Dethinne, T., and Malz, P.: Mass changes of the northern Antarctic Peninsula Ice Sheet derived from repeat bi-static synthetic aperture radar acquisitions for the period 2013–2017, The Cryosphere, 17, 4629–4644, https://doi.org/10.5194/tc-17-4629-2023, 2023.

Shahateet, K., Navarro, F., Seehaus, T., Fürst, J. J., and Braun, M.: Estimating ice discharge of the Antarctic Peninsula using different ice-thickness datasets, Annals of Glaciology, 64, 121–132, https://doi.org/10.1017/aog.2023.67, 2023.

Shepherd, A., Ivins, E., Rignot, E., Smith, B., van den Broeke, M., Velicogna, I., Whitehouse, P., Briggs, K., Joughin, I., Krinner, G., Nowicki, S., Payne, T., Scambos, T., Schlegel, N., A, G., Agosta, C., Ahlstrøm, A., Babonis, G., Barletta, V., Blazquez, A., Bonin, J., Csatho, B., Cullather, R., Felikson, D., Fettweis, X., Forsberg, R., Gallee, H., Gardner, A., Gilbert, L., Groh, A., Gunter, B., Hanna, E., Harig, C., Helm, V., Horvath, A., Horwath, M., Khan, S., Kjeldsen, K. K., Konrad, H., Langen, P., Lecavalier, B., Loomis, B., Luthcke, S., McMillan, M., Melini, D., Mernild, S., Mohajerani, Y., Moore, P., Mouginot, J., Moyano, G., Muir, A., Nagler, T., Nield, G., Nilsson, J., Noel, B., Otosaka, I., Pattle, M. E., Peltier, W. R., Pie, N., Rietbroek, R., Rott, H., Sandberg-Sørensen, L., Sasgen, I., Save, H., Scheuchl, B., Schrama, E., Schröder, L., Seo, K.-W., Simonsen, S., Slater, T., Spada, G., Sutterley, T., Talpe, M., Tarasov, L., van de Berg, W. J., van der Wal, W., van Wessem, M., Vishwakarma, B. D., Wiese, D., Wouters, B., and The IMBIE team: Mass balance of the Antarctic Ice Sheet from 1992 to 2017, Nature, 558, 219–222, https://doi.org/10.1038/s41586-018-0179-y, publisher: Nature Publishing Group, 2018.

Silva, A. B., Arigony-Neto, J., Braun, M. H., Espinoza, J. M. A., Costi, J., and Jaña, R.: Spatial and temporal analysis of changes in the glaciers of the Antarctic Peninsula, Global and Planetary Change, 184, 103 079, https://doi.org/10.1016/j.gloplacha.2019.103079, 2020.

Smith, B., Fricker, H. A., Gardner, A. S., Medley, B., Nilsson, J., Paolo, F. S., Holschuh, N., Adusumilli, S., Brunt, K., Csatho, B., Harbeck, K., Markus, T., Neumann, T., Siegfried, M. R., and Zwally, H. J.: Pervasive ice sheet mass loss reflects competing ocean and atmosphere processes, Science, 368, 1239–1242, https://doi.org/10.1126/science.aaz5845, 2020.

Soci, C., Hersbach, H., Simmons, A., Poli, P., Bell, B., Berrisford, P., Horányi, A., Muñoz-Sabater, J., Nicolas, J., Radu, R., Schepers, D., Villaume, S., Haimberger, L., Woollen, J., Buontempo, C., and Thépaut, J.: The ERA5 global reanalysis from 1940 to 2022, Quarterly Journal of the Royal Meteorological Society, 150, 4014–4048, https://doi.org/10.1002/qj.4803, 2024.

Stevens, C. M., Verjans, V., Lundin, J. M. D., Kahle, E. C., Horlings, A. N., Horlings, B. I., and Waddington, E. D.: The Community Firn Model (CFM) v1.0, Geoscientific Model Development, 13, 4355–4377, https://doi.org/10.5194/gmd-13-4355-2020, 2020.

Surawy-Stepney, T., Hogg, A. E., Cornford, S. L., Wallis, B. J., Davison, B. J., Selley, H. L., Slater, R. A. W., Lie, E. K., Jakob, L., Ridout, A., Gourmelen, N., Freer, B. I. D., Wilson, S. F., and Shepherd, A.: The effect of landfast sea ice buttressing on ice dynamic speedup in the Larsen B embayment, Antarctica, The Cryosphere, 18, 977–993, https://doi.org/10.5194/tc-18-977-2024, 2024.

The Firn Symposium team, Amory, C., Buizert, C., Buzzard, S., Case, E., Clerx, N., Culberg, R., Datta, R. T., Dey, R., Drews, R., Dunmire, D., Eayrs, C., Hansen, N., Humbert, A., Kaitheri, A., Keegan, K., Kuipers Munneke, P., Lenaerts, J. T. M., Lhermitte, S., Mair, D., McDowell, I., Mejia, J., Meyer, C. R., Morris, E., Moser, D., Oraschewski, F. M., Pearce, E., De Roda Husman, S., Schlegel, N.-J., Schultz, T., Simonsen, S. B., Stevens, C. M., Thomas, E. R., Thompson-Munson, M., Wever, N., and Wouters, B.: Firn on ice sheets, Nature Reviews Earth & Environment, 5, 79–99, https://doi.org/10.1038/s43017-023-00507-9, 2024.

Toutin, T., Schmitt, C., Berthier, E., and Clavet, D.: DEM generation over ice fields in the Canadian Arctic with along-track SPOT5 HRS stereo data, Canadian Journal of Remote Sensing, 37, 429–438, https://doi.org/10.5589/m11-052, 2011.

https://doi.org/10.5194/egusphere-2026-729
Preprint. Discussion started: 3 March 2026

van Wessem, J. M., van de Berg, W. J., Noël, B. P. Y., van Meijgaard, E., Amory, C., Birnbaum, G., Jakobs, C. L., Krüger, K., Lenaerts, J. T. M., Lhermitte, S., Ligtenberg, S. R. M., Medley, B., Reijmer, C. H., van Tricht, K., Trusel, L. D., van Ulft, L. H., Wouters, B., Wuite, J., and van den Broeke, M. R.: Modelling the climate and surface mass balance of polar ice sheets using RACMO2 – Part 2: Antarctica (1979–2016), The Cryosphere, 12, 1479–1498, https://doi.org/10.5194/tc-12-1479-2018, 2018.

Veldhuijsen, S., Willem, J. v. d. B., Michiel R., v. d. B., and Peter, K. M.: IMAU-FDM v1.2A variables over Antarctica (1979-2023), https://doi.org/10.5281/zenodo.14634258, 2025.

Veldhuijsen, S. B. M., van de Berg, W. J., Brils, M., Kuipers Munneke, P., and van den Broeke, M. R.: Characteristics of the 1979–2020 Antarctic firn layer simulated with IMAU-FDM v1.2A, The Cryosphere, 17, 1675–1696, https://doi.org/10.5194/tc-17-1675-2023, publisher: Copernicus GmbH, 2023.

Wallis, B. J., Hogg, A. E., Meredith, M. P., Close, R., Hardy, D., McMillan, M., Wuite, J., Nagler, T., and Moffat, C.: Ocean warming drives rapid dynamic activation of marine-terminating glacier on the west Antarctic Peninsula, Nature Communications, 14, 7535, https://doi.org/10.1038/s41467-023-42970-4, 2023.

Wang, W., Shen, Y., Chen, Q., and Wang, F.: Unprecedented mass gain over the Antarctic ice sheet between 2021 and 2022 caused by large precipitation anomalies, Environmental Research Letters, 18, 124 012, https://doi.org/10.1088/1748-9326/ad0863, 2023.

Whitehouse, P. L., Bentley, M. J., Milne, G. A., King, M. A., and Thomas, I. D.: A new glacial isostatic adjustment model for Antarctica: calibrated and tested using observations of relative sea-level change and present-day uplift rates, Geophysical Journal International, 190, 1464–1482, 2012.

Wouters, B., Martin-Español, A., Helm, V., Flament, T., Van Wessem, J. M., Ligtenberg, S. R. M., Van Den Broeke, M. R., and Bamber, J. L.: Dynamic thinning of glaciers on the Southern Antarctic Peninsula, Science, 348, 899–903, https://doi.org/10.1126/science.aaa5727, 2015.

Zhao, C., King, M. A., Watson, C. S., Barletta, V. R., Bordoni, A., Dell, M., and Whitehouse, P. L.: Rapid ice unloading in the Fleming Glacier region, southern Antarctic Peninsula, and its effect on bedrock uplift rates, Earth and Planetary Science Letters, 473, 164–176, https://doi.org/https://doi.org/10.1016/j.epsl.2017.06.002, 2017.

Zwally, H., Schutz, B., Abdalati, W., Abshire, J., Bentley, C., Brenner, A., Bufton, J., Dezio, J., Hancock, D., Harding, D., Herring, T., Minster, B., Quinn, K., Palm, S., Spinhirne, J., and Thomas, R.: ICESat's laser measurements of polar ice, atmosphere, ocean, and land, Journal of Geodynamics, 34, 405–445, https://doi.org/10.1016/S0264-3707(02)00042-X, 2002.

Zwally, H., Schutz, R., Hancock, D., and Dimarzio, J.: GLAS/ICESat L2 Global Antarctic and Greenland Ice Sheet Altimetry Data (HDF5), Version 34, https://doi.org/10.5067/ICESAT/GLAS/DATA209, 2014.

Zwally, J., Giovinetto, M., Beckley, M., and Saba, J.: Antarctic and Greenland Drainage Systems, GSFC Cryospheric Sciences Laboratory, https://doi.org/10.1016/j.rse.2016.12.029https://earth.gsfc.nasa.gov/cryo/data/ polar-altimetry/antarctic-and-greenland-drainage-systems, 2012.